



Experimental Study of Mechanical and Permeability Behaviors During the Failure of Sandstone Containing Two Preexisting Fissures Under Triaxial Compression

Yiteng Du¹ · Tingchun Li¹ · Weiteng Li¹ · Yande Ren² · Gang Wang¹ · Peng He¹

Received: 27 June 2019 / Accepted: 7 April 2020 / Published online: 28 April 2020
© Springer-Verlag GmbH Austria, part of Springer Nature 2020

Abstract

Rock masses are typical inhomogeneous geological materials that contain many fissures and cracks. The coupling effect of the crack propagation and seepage evolution in rocks is very important to the safety of rock engineering. However, hydromechanical coupling behavior during the failure of fissured rocks has rarely been investigated. In this research, hydromechanical coupling tests are performed to fully explore the behaviors in strength, deformation, permeability and failure mode of sandstone samples with two preexisting fissures. The experimental results show that the ratio of crack initiation threshold/peak strength, the ratio of crack damage threshold/peak strength and the value of the elastic modulus decrease by at most 31.8%, 12.2% and 18.4% due to the existence of the two fissures, while the Poisson's ratio increases by at most 45.6%. Furthermore, the values of permeability before the sudden increase stage range from 2.1% to 17.6% of the maximum permeability value. The influence of bridge length and angle on permeability is more significant under lower confining pressure or higher water pressure. Five failure modes are observed in the double-fissure samples under hydromechanical coupling conditions. Additionally, the “wing cracks + indirect coalescence” failure mode is generated only when the ligament length is shorter than the fissure length. The corresponding strength is lower than that for other failure modes. CT images show that the expansion of cracks inside the samples is more restricted than that at the surface of the samples, especially near the rock bridge region. The effects of failure modes on the mechanical and permeability properties, from greatest to least, are as follows: crack initiation threshold, peak strength, crack damage threshold, elastic modulus, Poisson's ratio and permeability. This research is contributed to analyze the stability of water-bearing rocks in underground caverns with many preexisting fissures.

Keywords Sandstone · Preexisting fissure · Hydromechanical coupling tests · Mechanical properties · Permeability · Failure behavior

List of Symbols

W Wing crack
AW Anti-wing crack
INC Indirect coalescence
SC Secondary crack
NC No coalescence
DC Direct coalescence
UCS Uniaxial compression strength

ρ Density
 n Initial porosity
 σ_t Tensile strength
 E Elastic modulus
 μ Poisson's ratio
 C Cohesion
 φ Friction angle
 K Softening factor
 k Permeability
 Q Water flow rate
 A Cross-sectional area of the sample
 μ_f Dynamic viscosity of the fluid
 ΔP Water pressure difference applied between both end planes of the rock sample
 H Height of sample
 D Diameter of sample
 a Half-length of the fissure

✉ Tingchun Li
tchli_sd@163.com

¹ Shandong Key Laboratory of Civil Engineering Disaster Prevention and Mitigation, Shandong University of Science and Technology, Qingdao 266590, China

² Radiology Department, The Affiliated Hospital of Qingdao University, Qingdao 266590, China

b	Width of the fissure
α	Fissure dip angle
L	Rock bridge ligament length
β	Rock bridge angle
P_c	Confining pressure
P_w	Water pressure
ε_1	Axial strain
ε_3	Lateral strain
ε_v	Volumetric strain
ε_{vc}	Crack-induced volumetric strain
σ_1	Axial stress
σ_3	Confining pressure
σ_{cc}	Primary crack closure threshold
σ_{ci}	Crack initiation threshold
σ_{cd}	Crack damage threshold
σ_c	Peak strength
σ_r	Residual strength
k_0	Initial permeability
k_{ci}	Permeability corresponding to the crack initiation threshold
k_{cd}	Permeability corresponding to the crack damage threshold
k_c	Permeability corresponding to the peak strength
k_{max}	Maximum permeability

1 Introduction

Rock masses contain many fissures and cracks that originate from diagenetic processes, tectonic processes and excavation disturbance (Prudencio and Van 2007; Yin et al. 2014; Li et al. 2015; Wang et al. 2019; Li et al. 2020). The initiation and propagation of cracks in rocks have a significant effect on the strength, deformability and failure behaviors of rock masses (Yang et al. 2008; Janeiro and Einstein 2010; Lee and Jeon 2011; Bahaaddini et al. 2013; Zhou et al. 2014). Additionally, problems associated with groundwater constitute an important obstacle in the stability of rock engineering. Furthermore, the coupling effects of crack propagation and seepage will further induce the unstable failure of the rock mass, which may pose a threat to the construction safety of rock engineering structures. Therefore, studies on the mechanical and permeability characteristics of fissured rocks under hydromechanical coupling conditions are crucial for controlling the stability of rock engineering involving jointed rocks.

In previous studies, extensive compression tests (Lu et al. 2014, 2015; Yang et al. 2018; Wu et al. 2019; Huang et al. 2019; Haeri et al. 2014; Cao et al. 2015; Zhao et al. 2019; Zhou et al. 2019) and numerical simulations (Wong and Li 2013; Wang et al. 2014b; Fu et al. 2016, 2017; Lee et al. 2017) have been conducted to investigate the mechanical behavior and failure in rock and rock-like specimens

containing preexisting fissures. New cracks are generally initiated at the tips of preexisting fissures when the stress reaches the crack initiation threshold. Additionally, these cracks can be divided into tensile cracks, shear cracks and mixed tensile-shear cracks (Wong and Einstein 2009; Park and Bobet 2010; Yang et al. 2017; Yang and Huang 2017; Wang et al. 2018). To gain a better understanding of the effects of fissure geometry (fissure angle, bridge angle, and geometry length) on crack coalescence, researchers, such as Morgan et al. (2013), Zhao et al. (2016), Afolagboye et al. (2018), conducted uniaxial compression tests on rock and rock-like specimens containing two fissures. The results showed that more direct coalescence between the fissures was observed with increasing bridge angle and fissure angle. As the ligament length increased, the coalescence behavior changed from direct coalescence to indirect coalescence and then to no coalescence. Similarly, Huang et al. (2016a) carried out triaxial compression tests on sandstone with three types of preexisting pairs of flaws. They found that the stress–strain curves for a certain type of flawed rock sample show similar trends. In addition, the stress required for crack initiation and the critical stress of dilation are close to the peak strength of the specimen, and a smaller difference between these two stresses results from an increase in the confining pressure. Huang et al. (2016b) used the numerical software PFC3D to investigate the cracking behavior of rock-like specimens containing two nonparallel fissures under conventional triaxial compression. They found that the failure mode is mainly affected by the fissure angle at a small confining pressure, but it is mainly influenced by the confining pressure at a high confining pressure.

To investigate the permeability characteristics of rocks, many hydromechanical coupling tests have been conducted on intact granite (Sun et al. 2015; Wang et al. 2016a), limestone (Zhang et al. 2013; Wang et al. 2015) and sandstone specimens (Yu et al. 2015; Chen 2016; Wang et al. 2016b; Chen et al. 2018). The results showed that the failure of intact rock specimens is caused mainly by the formation of a shear fracture through the top and bottom boundaries. Furthermore, the evolution of permeability varies with the stages of rock fracturing during the process of compression. Chen et al. (2017) found that the influence of confining pressures on stress–strain behaviour, permeability evolution and failure pattern of intact sandstone samples is much greater than that of water pressure, based on their experimental and RFPA2D simulation results. Cai et al. (2018) and Zeng et al. (2018) investigated the permeability and failure of intact rocks using PFC2D software. They found that changes in the mesoscopic structure, accumulated damage and permeability of rock samples under hydromechanical coupling conditions produce obvious synergistic effects. Furthermore, the pore pressure and flow rate both preferentially transmit through

the damage zones in the specimens rather than the intact rock matrix during steady flow.

In the past, theoretical research on the coupling effect of crack propagation and seepage evolution of rocks has been limited. The main contributions of most of the previous experimental and numerical studies on the failure mechanism and permeability behavior of rock are mainly limited to uniaxial or triaxial compression tests on pre-cracked samples and permeability evolution analysis of intact samples. Additionally, the changes in the mechanical, permeability and failure characteristics of rocks containing preexisting fissures under hydromechanical coupling conditions have rarely been investigated. Consequently, the hydromechanical behavior during the failure of rocks that contain preexisting fissures is not fully understood. In the present study, a series of hydromechanical coupling tests on sandstone samples containing two preexisting fissures with various ligament lengths and bridge angles were carried out. Based on the experimental results, the combined influences of the confining pressure, water pressure, ligament length and bridge angle on the strength, deformability and permeability characteristics are first investigated. Then, the failure of sandstone samples that include a rock bridge (5 rock bridge types are considered) is studied under various confining pressures and water pressures. Simultaneously, the post-test internal crack patterns of the sandstone samples are revealed by computed tomography (CT) imaging. Finally, the strength, deformation and permeability characteristics corresponding to various failure modes are analyzed in detail.

2 Experimental Material and Procedure

2.1 Sandstone Material and Preparation of Samples

The samples used in the present experimental study are red sandstone collected from a quarry in Tai'an city in eastern China. This sandstone exhibits good homogeneity. Additionally, the mineral components of the tested sandstone according to X-ray diffraction (XRD) analysis are shown in Table 1.

Table 1 Mineral components of the tested sandstone

Minerals	Feldspar	Quartz	Montmorillonite
Percentage	74.2%	13.0%	12.8%

Table 2 Properties of the tested sandstone

Properties	ρ (kg/m ³)	n (%)	k_0 (m ²)	σ_t (MPa)	UCS (MPa)	E (GPa)	μ	C (MPa)	φ (°)	K
Value	2392	7.55	10 ⁻¹⁸ -10 ⁻¹⁷	4.78	73.07	22.35	0.31	27.08	34.48	0.71

ρ density, n initial porosity, k_0 initial permeability, σ_t tensile strength, UCS uniaxial compressive strength, E elastic modulus, μ Poisson's ratio, C cohesion, φ friction angle, K softening factor

Furthermore, the properties of the tested sandstone based on the laboratory testing analysis are shown in Table 2. After cutting and polishing, cylindrical samples 100 mm in length and 50 mm in diameter were prepared according to the method suggested by the International Society for Rock Mechanics (ISRM). Then, two fissures with the same length (10 mm) and width (1.5 mm) were produced in the samples, and the production procedure is as follows (as shown in Fig. 1): (1) drill two holes through the sandstone sample by using a diamond drill with diameter 1.5 mm at the position where the fissures need to be produced in the samples; (2) install the production mold on the sandstone sample with two holes, and the holes on the sandstone sample must be located in the slits with length 10 mm and width 1.5 mm on the mold; and (3) pass the diamond wire saw with diameter 1.0 mm through the small hole, and pull the saw back and forth along the slit on the mold until the fissure is completely produced. In addition, the geometry and location of the fissures are shown in Fig. 2a. The tested sandstone samples were saturated with tap water under vacuum by using a vacuum pump, as shown in Fig. 2b, before mounting in the triaxial cell. To investigate the hydromechanical behavior of these double-fissure sandstone samples, three confining pressures (5, 10, and 15 MPa) and three water pressures (2, 5, and 8 MPa) were chosen. Three sets of samples are selected for testing in each group to obtain optimal results. A detailed description of the tested sandstone samples is listed in Table 3.

2.2 Testing Equipment and Procedure

The hydromechanical coupling tests were carried out with the TAW-2000 electrohydraulic servo-controlled testing equipment in Shandong Key Laboratory of Civil Engineering Disaster Prevention and Mitigation at Shandong University of Science and Technology in China, as shown in Fig. 3a. The testing equipment consists of three separate control systems for the axial pressure, confining pressure, and water pressure. The axial and radial deformation were measured simultaneously by the axial and radial displacement gauges with a measuring capacity of 0–4 mm and a reading accuracy of $\pm 1\%$ at room temperature, as shown in Fig. 3c. The data were collected automatically by the digitized computer configuration. The reading of the axial displacement was also used as a feedback signal for the external load control. Additionally, the axial displacement rate was set to a constant value on the control system. This

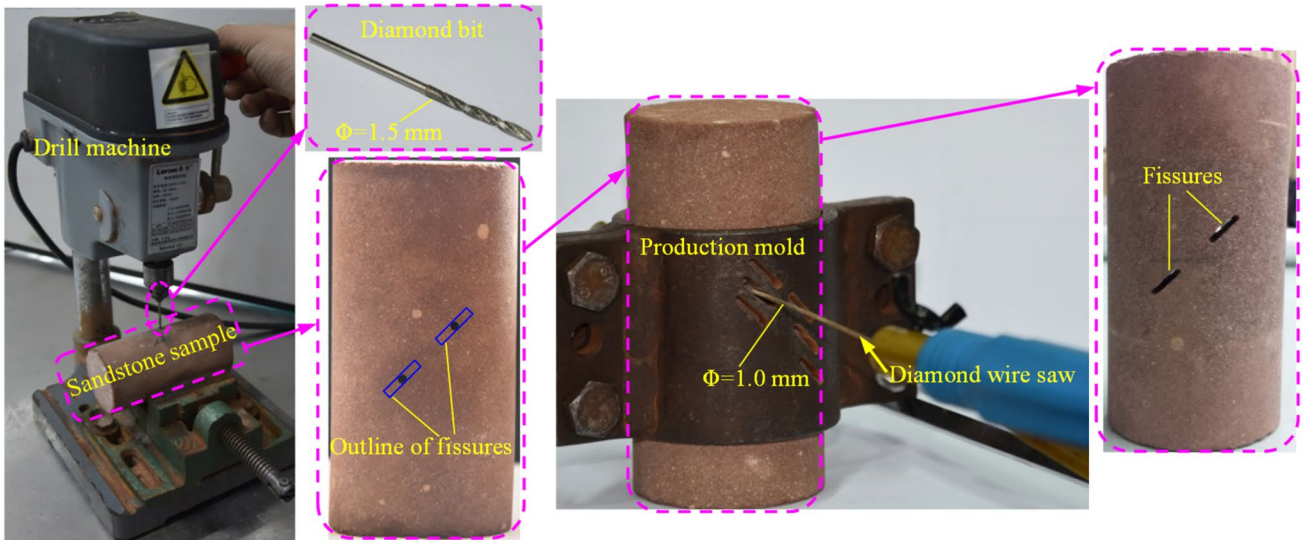


Fig. 1 Production of sandstone samples with two fissures

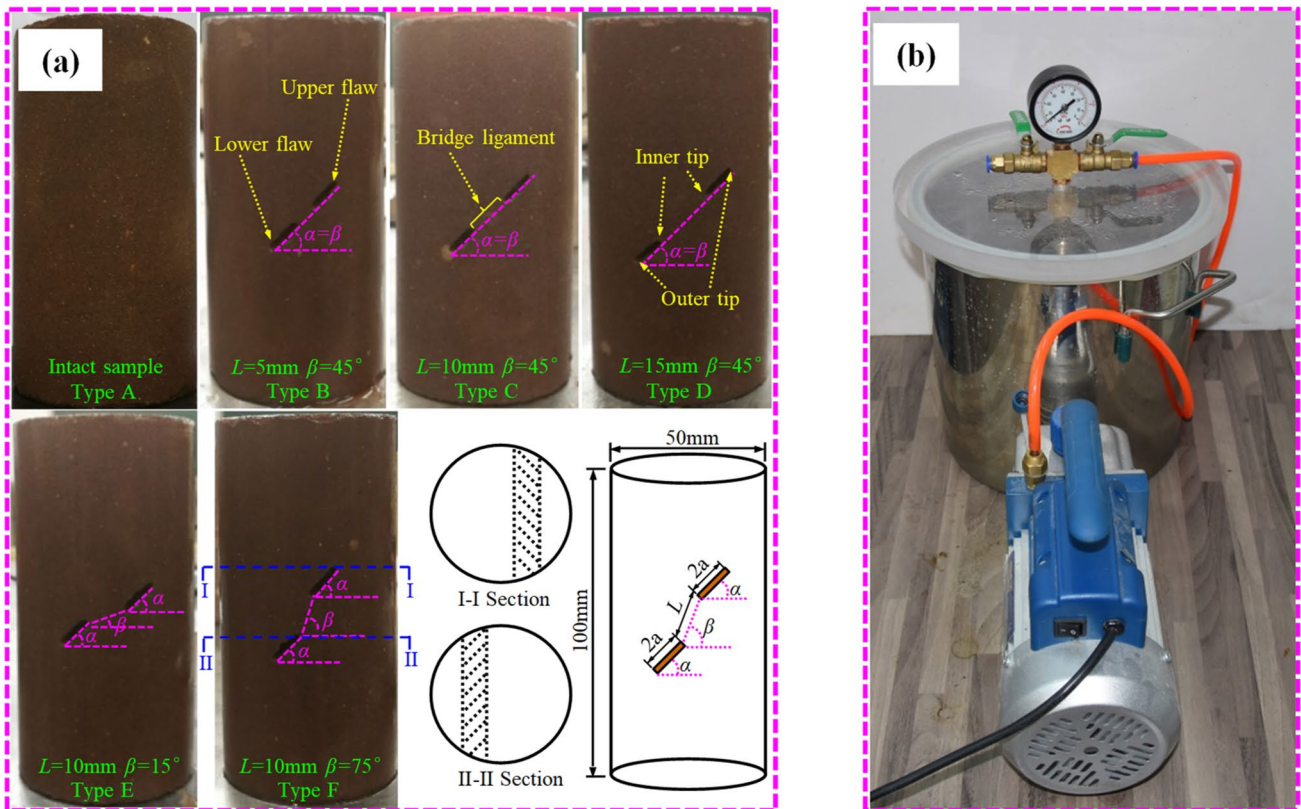


Fig. 2 Diagrams of the tested sandstone samples and vacuum pump: **a** tested sandstone and **b** vacuum pump

function can effectively control the loading in the complete stress–strain process (including the strain-softening stage).

The experimental procedure, which is similar to Wang et al. (2014a, 2016b), Chen et al. (2017), Zhao et al. (2017), is as follows:

Table 3 Tested sandstone samples with or without a single fissure

Sample number	<i>H</i> (mm)	<i>D</i> (mm)	<i>2a</i> (mm)	<i>b</i> (mm)	α (°)	<i>L</i> (mm)	β (°)	<i>P_c</i> (MPa)	<i>P_w</i> (MPa)	Comment
A-00-2 [#]	99.86	49.78	–	–	–	–	–	0	0	Intact samples
A-52-1 [#]	99.92	49.42	–	–	–	–	–	5	2	
A-102-3 [#]	100.24	49.46	–	–	–	–	–	10	2	
A-152-2 [#]	99.86	49.52	–	–	–	–	–	15	2	
A-155-2 [#]	100.04	49.88	–	–	–	–	–	15	5	
A-158-2 [#]	100.18	49.76	–	–	–	–	–	15	8	
B-00-1 [#]	99.54	49.62	10	1.5	45	5	45	0	0	Samples with two parallel pre-existing fissures
B-52-1 [#]	99.86	49.34	10	1.5	45	5	45	5	2	
B-102-1 [#]	99.82	49.58	10	1.5	45	5	45	10	2	
B-152-2 [#]	99.74	49.22	10	1.5	45	5	45	15	2	
B-155-1 [#]	99.52	49.74	10	1.5	45	5	45	15	5	
B-158-2 [#]	99.98	49.38	10	1.5	45	5	45	15	8	
C-00-3 [#]	99.26	49.26	10	1.5	45	10	45	0	0	
C-52-1 [#]	99.78	49.92	10	1.5	45	10	45	5	2	
C-102-2 [#]	99.54	49.58	10	1.5	45	10	45	10	2	
C-152-2 [#]	99.84	49.34	10	1.5	45	10	45	15	2	
C-155-1 [#]	99.76	49.66	10	1.5	45	10	45	15	5	
C-158-3 [#]	99.62	49.36	10	1.5	45	10	45	15	8	
D-00-1 [#]	99.64	49.82	10	1.5	45	15	45	0	0	
D-52-1 [#]	99.38	49.54	10	1.5	45	15	45	5	2	
D-102-1 [#]	99.44	49.86	10	1.5	45	15	45	10	2	
D-152-1 [#]	99.92	49.46	10	1.5	45	15	45	15	2	
D-155-1 [#]	99.28	49.24	10	1.5	45	15	45	15	5	
D-158-3 [#]	99.52	49.82	10	1.5	45	15	45	15	8	
E-00-3 [#]	99.74	49.76	10	1.5	45	10	15	0	0	
E-52-2 [#]	99.68	49.88	10	1.5	45	10	15	5	2	
E-102-3 [#]	99.76	49.22	10	1.5	45	10	15	10	2	
E-152-1 [#]	99.88	49.36	10	1.5	45	10	15	15	2	
E-155-3 [#]	99.64	49.74	10	1.5	45	10	15	15	5	
E-158-3 [#]	99.78	49.48	10	1.5	45	10	15	15	8	
F-00-1 [#]	99.68	49.56	10	1.5	45	10	75	0	0	
F-52-1 [#]	99.72	49.24	10	1.5	45	10	75	5	2	
F-102-1 [#]	99.36	49.82	10	1.5	45	10	75	10	2	
F-152-3 [#]	99.94	49.98	10	1.5	45	10	75	15	2	
F-155-3 [#]	99.28	49.66	10	1.5	45	10	75	15	5	
F-158-2 [#]	99.42	49.52	10	1.5	45	10	75	15	8	

H height of sample, *D* diameter of sample, *2a* length of fissure, *b* width of fissure, α fissure dip angle, *L* rock bridge ligament length, β rock bridge ligament angle, *P_c* confining pressure, *P_w* water pressure

1. The tested sandstone samples were saturated with tap water under vacuum by using a vacuum pump, as shown in Fig. 2b. To ensure complete saturation of the sandstone samples, the masses of the tested samples were measured regularly until staying constant.
2. The saturated tested sandstone samples were circumferentially wrapped in a shrinkable plastic sleeve to separate the confining pressure from the water pressure, as shown in Fig. 3c, d.
3. The assembled sandstone samples were mounted with both axial and circumferential deformation measurement devices to collect deformation data, as shown in Fig. 3c, and inserted into the triaxial cell.
4. The triaxial cell was lowered and filled with hydraulic oil, as shown in Fig. 3b. Then, the confining pressure induced by hydraulic oil was gradually increased to the required value. When the hydrostatic stress state, which is a stable state, is reached, the inlet water pressure at

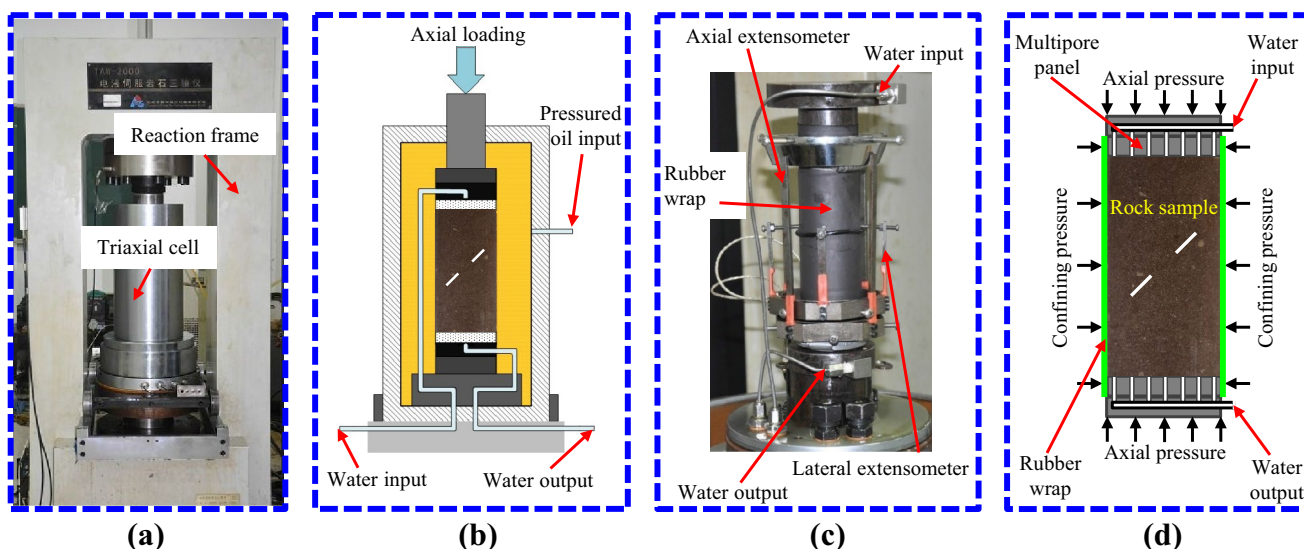


Fig. 3 Testing equipment and assembled sample: **a** TAW-2000 electrohydraulic servo-controlled testing equipment; **b** simplified schematic of triaxial cell; **c** installation of rock sample; **d** simplified schematic of the assembled sample

the upstream end of the sample was gradually applied to a predetermined value, and the outlet was open to the atmosphere. The outlet volumetric water flow rate at the downstream end of the sample was measured in real time by a water flow meter on the testing system.

- When the flow rate reached a constant value, the axial stress was increased under constant axial displacement control at a rate of 0.02 mm/min, and the confining pressure and water pressure were kept constant throughout the experiment.

Generally, there are two main experimental methods used to measure the permeability of rocks during triaxial compression: steady-state flow tests and transient (or pulse) tests (Brace et al. 1968; Oda et al. 2002; Davy et al. 2007; Chen et al. 2017). When the permeability $k \geq 10^{-19} \text{ m}^2$, the steady-state flow tests are more suitable (Davy et al. 2007; Chen et al. 2017). In this research, the steady-state flow tests were chosen due to that the initial permeability of the tested sandstone is approximately 10^{-18} – 10^{-17} m^2 . Darcy's law is usually assumed to be valid for steady-state flow tests, which can calculate the absolute permeability by the measured flow rate and the water pressure difference applied between both end planes of the rock sample. Here, Darcy's law can be written as follows (Wyckoff et al. 1933; Zhao et al. 2017; Chen et al. 2017):

$$k = \frac{Q\mu_f H}{\Delta p A}, \quad (1)$$

where k is the permeability (m^2); Q is the water flow rate (m^3/s); A is the cross-sectional area of the sample (m^2); μ_f is the dynamic viscosity of the fluid, where the μ_f value of water at room temperature is $1.005 \times 10^{-3} \text{ Pa s}$; H is the height of the sample (m); and Δp is the water pressure difference applied between both end planes of the rock sample.

3 Experimental Results

3.1 Characteristics of Stress–Strain Curves

3.1.1 Stress–Strain Curves Under Different Confining Pressures

The stress–strain curves of intact and double-fissure sandstone with five different bridge ligaments under different confining pressures are shown in Fig. 4. The lateral strain of all the tested samples in the initial loading stage is close to zero and considerably smaller than the corresponding axial strain under different confining pressures. The slope of the pre-peak stress versus axial strain curve is positively correlated with confining pressure. The axial stress drops sharply to a value close to zero after the peak strength is reached under uniaxial compression but drops to the residual strength, with some fluctuations (especially

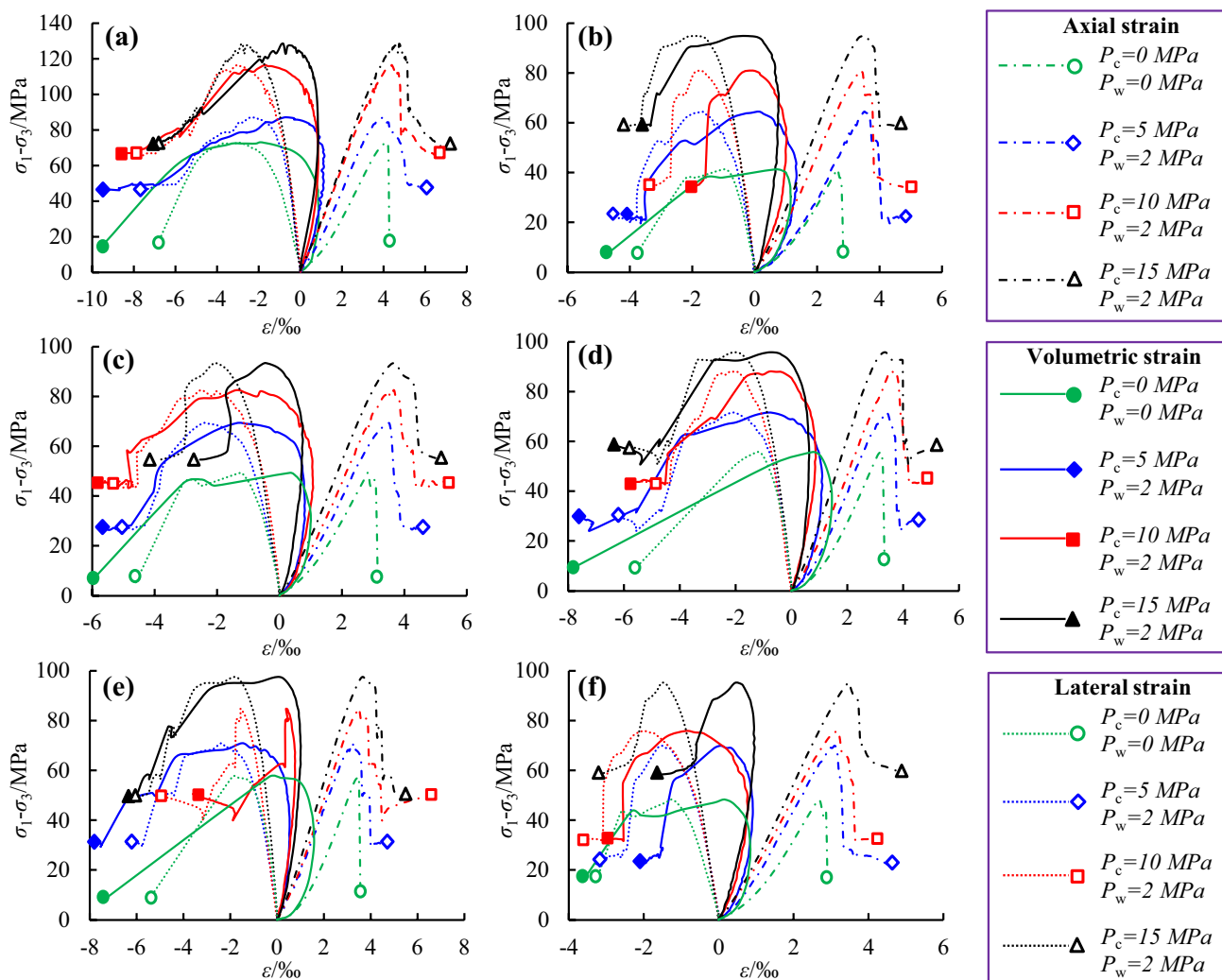


Fig. 4 Stress–strain curves of tested samples under different confining pressures: **a** intact sample; **b** $L=5$ mm and $\beta=45^\circ$; **c** $L=10$ mm and $\beta=45^\circ$; **d** $L=15$ mm and $\beta=45^\circ$; **e** $L=10$ mm and $\beta=15^\circ$; and **f** $L=10$ mm and $\beta=75^\circ$

when $L=10$ mm and $\beta=15^\circ$), under different confining pressures. The peak and residual strengths decrease with decreasing confining pressure, but the increase in the axial strain in the softening stage is negatively correlated with the confining pressure. In addition, the two fissures with various bridge geometries have remarkable effects on the strength and deformability characteristics of sandstone, especially under lower confining pressures.

3.1.2 Stress–Strain Curves Under Different Water Pressures

Figure 5 describes the stress–strain curves of intact and double-fissure sandstone samples under different water pressures. When the confining pressure is constant at 15 MPa, the shapes of the stress–strain curves of intact samples exhibit no obvious changes, regardless of the applied water pressure. However, the slopes of the stress versus axial strain

curves of the double-fissure samples with different bridge ligaments decrease gradually in the plastic deformation stages, while the lateral deformability and volume significantly increase with increasing water pressure. Moreover, the peak and residual strengths are negatively correlated with water pressure. Furthermore, the influence of water pressure on the strength and deformability of double-fissure sandstone is mostly concentrated in the plastic and post-peak segments.

3.2 Strength Properties

In general, the failure process of rocks during compression can be divided into five stages (Bieniawski 1967; Tang et al. 2019): (1) crack closure, (2) linear elastic deformation, (3) crack initiation and stable crack growth, (4) critical energy release and unstable crack growth, and (5) failure and

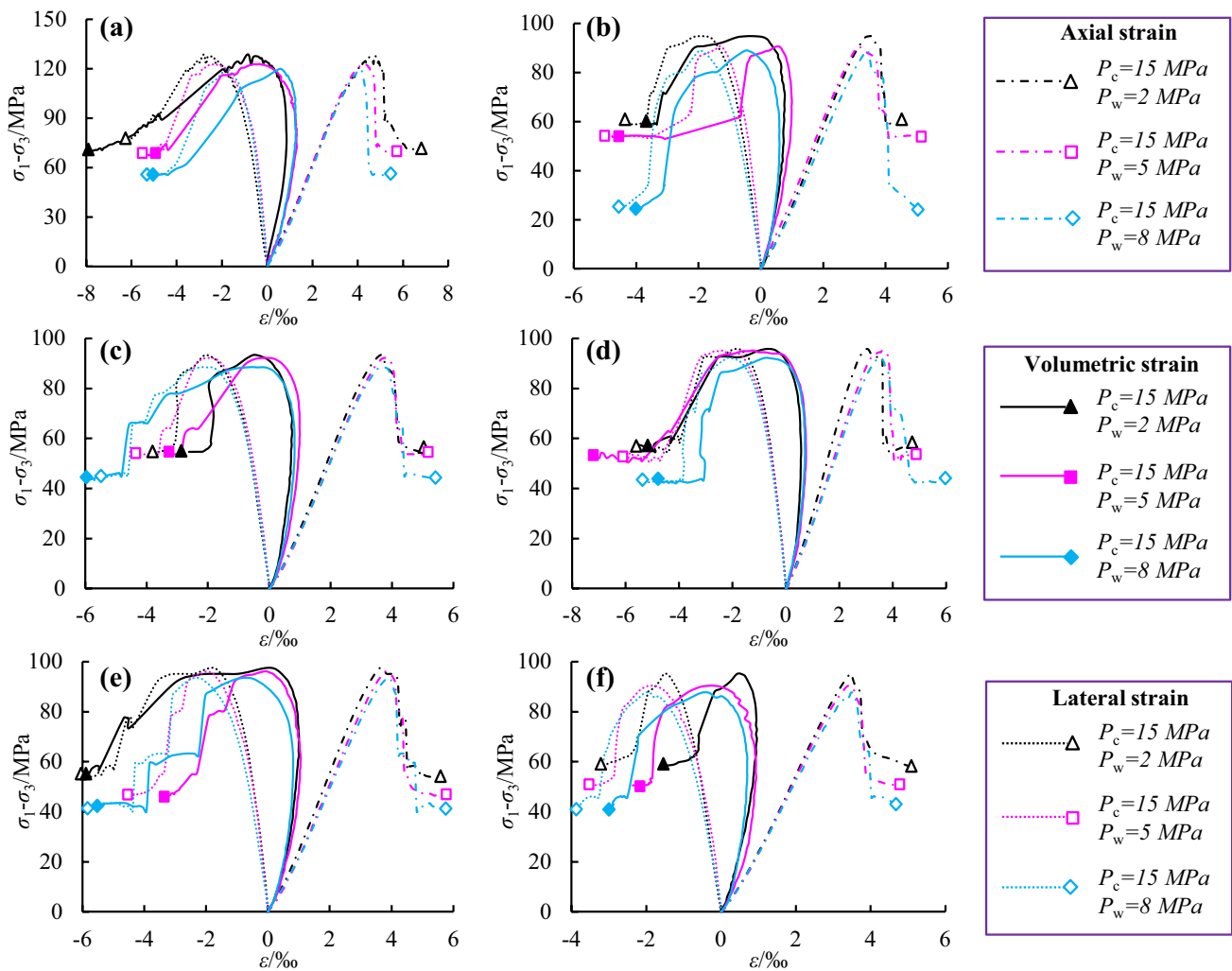


Fig. 5 Stress–strain curves of the tested samples under different water pressures: **a** intact sample; **b** $L=5$ mm and $\beta=45^\circ$; **c** $L=10$ mm and $\beta=45^\circ$; **d** $L=15$ mm and $\beta=45^\circ$; **e** $L=10$ mm and $\beta=15^\circ$; and **f** $L=10$ mm and $\beta=75^\circ$

post-peak behavior based on the stress–strain behavior of a loaded rock sample. Martin and Chandler 1994 defined the primary crack closure threshold σ_{cc} , crack initiation threshold σ_{ci} , crack damage threshold σ_{cd} , and peak strength σ_c to divide the five stages in the stress–strain curves of rocks under compression, especially for σ_{ci} and σ_{cd} , as shown in Fig. 6. Afterwards, many researchers, such as Eberhardt et al. 1998; Cai et al. 2004; Yu et al. 2015; Huang et al. 2016a; Tang et al. 2019, have investigated the fracture evolution of rocks under uniaxial and triaxial compression based on a method modified from Martin and Chandler 1994. In this research, we have also used the above method and mainly investigated the crack initiation threshold σ_{ci} , crack damage threshold σ_{cd} , peak strength σ_c and residual strength σ_r during the failure of sandstone containing two preexisting fissures under hydromechanical coupling conditions. Here, the crack initiation threshold σ_{ci} corresponds to the axial

deviatoric stress at the inflection of the stress–strain curve from the crack-induced volumetric strain ε_{vc} to the axial strain ε_1 ; at this inflection point, the value of ε_{vc} changes from increasing to decreasing with ε_1 . Additionally, the crack damage threshold σ_{cd} corresponds to the axial deviatoric stress at the inflection of the stress–strain curve from the volumetric strain ε_v to the axial strain ε_1 ; at this inflection point, the value of ε_v begins to decrease with ε_1 . The crack-induced volumetric strain ε_{vc} and the volumetric strain ε_v can be calculated as follows (Yu et al. 2015):

$$\varepsilon_{vc} = \varepsilon_v - \frac{1-2\mu}{E}(\sigma_1 + 2\sigma_3) \quad (2)$$

$$\varepsilon_v = \varepsilon_1 + 2\varepsilon_3, \quad (3)$$

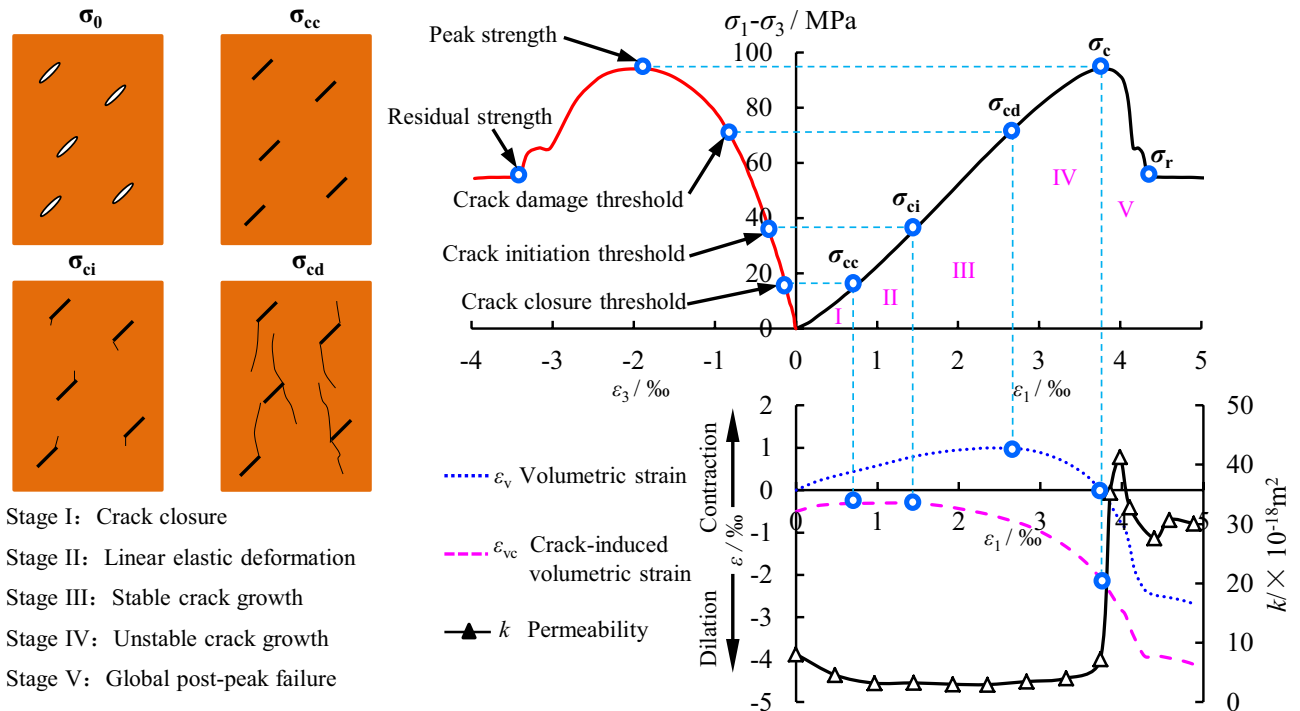


Fig. 6 Typical stress–strain curves of rocks under triaxial compression (modified from Martin and Chandler 1994)

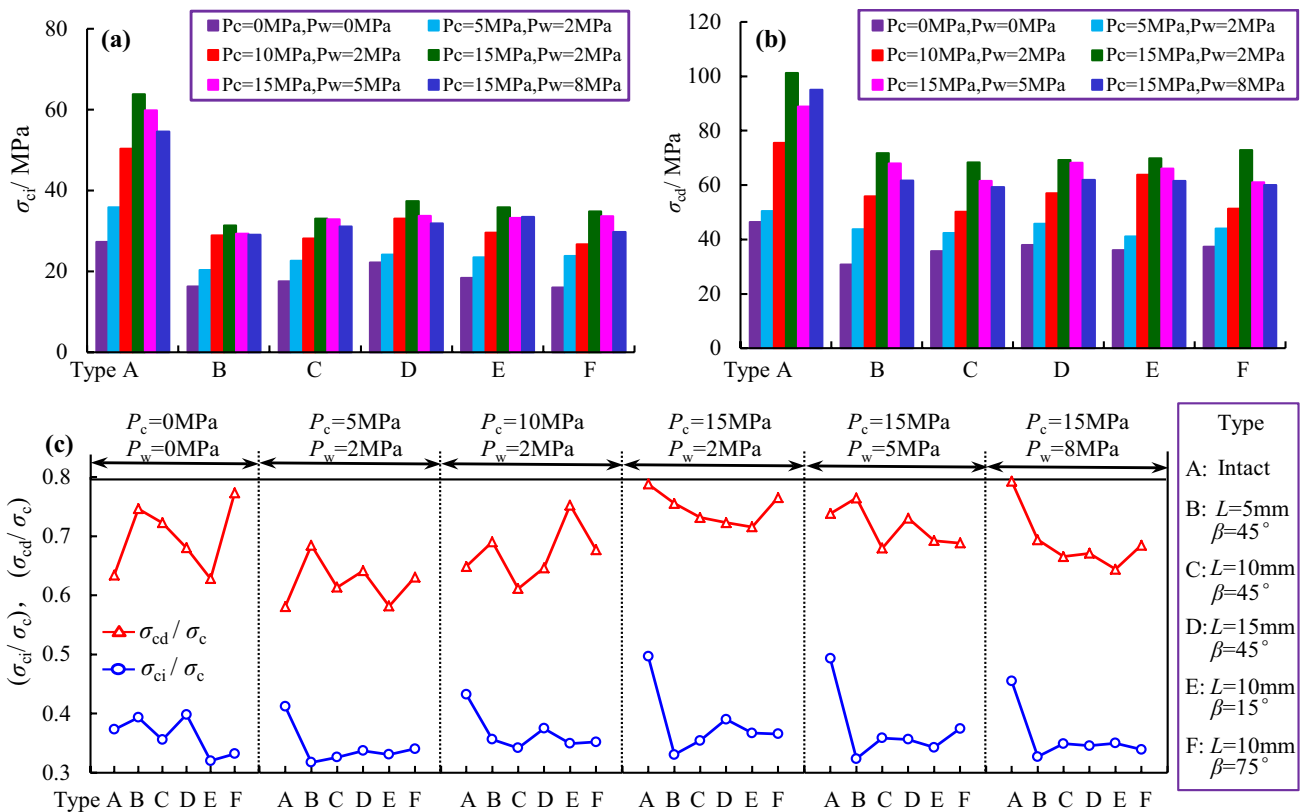


Fig. 7 Crack initiation threshold and crack damage threshold of the tested samples: **a** crack initiation threshold; **b** crack damage threshold; and **c** ratios of the crack initiation threshold and crack damage threshold to the peak strength

where μ denotes Poisson's ratio, E denotes the elastic modulus, σ_1 denotes the axial stress, and σ_3 denotes the confining pressure, ε_1 denotes the axial strain, ε_3 denotes the lateral strain.

3.2.1 Crack Initiation and Crack Damage Thresholds

Figure 7 presents the crack initiation threshold σ_{ci} , crack damage threshold σ_{cd} and ratios of σ_{ci} and σ_{cd} to the peak strength σ_c of the tested samples.

The values of σ_{ci} and σ_{cd} of all the samples tested under uniaxial compressions decrease by 20.3%–57.2% and 8.2%–57.1%, respectively, compared with those under various confining pressures (5, 10, and 15 MPa) and water pressures (2, 5, and 8 MPa). When the confining pressure is constant at 15 MPa, the values of σ_{ci} and σ_{cd} of all tested samples decrease by 6.1%–14.7% and 6.0%–17.7%, respectively, due to the increase in water pressure from 2 to 8 MPa.

The value of σ_{ci}/σ_c of the double-fissure samples fluctuates from 0.320 to 0.394 under uniaxial compression, but it is clearly lower than that of the intact samples under the confining pressure and water pressure coupled conditions. Furthermore, the values of σ_{ci}/σ_c and σ_{cd}/σ_c increase by 4.1%–15.8% and 10.7%–23.3% after the confining pressure increases by two times, but decrease by 1.0%–11.5% and 7.2%–10.6% after the water pressure increases by three times. Therefore, the influence of confining pressure is greater than that of water pressure on the strength parameters. Additionally, the influence of the confining pressure, water pressure, ligament length and bridge angle on the crack damage threshold is more remarkable than that on the crack initiation threshold.

3.2.2 Peak Strength

Figure 8 shows the peak strengths of the double-fissure samples under uniaxial compression and hydromechanical coupling conditions. The peak strengths of double-fissure samples under uniaxial compression are 19.0%–56.6% less than those under coupled hydromechanical conditions; the greatest drop occurs in the sample with $L=5$ mm and $\beta=45^\circ$. Additionally, the influence of the ligament length and bridge angle on the peak strength under higher confining pressures is lower than that under uniaxial compression. Furthermore, the peak strength increases by 34.8%–47.4% after the confining pressure increases by two times. However, the peak strength decreases by 2.1%–8.0% after the water pressure increases by three times, indicating that the influence of confining pressure is greater than that of water pressure on the peak strength.

3.2.3 Residual Strength

Figure 9 shows the residual strength of the double-fissure samples under hydromechanical coupling conditions.

In Fig. 9a, it can be seen that the residual strengths of the double-fissure samples decrease by 40.9%–58.5% at $P_c=5$ MPa and $P_w=2$ MPa, decrease by 33.1%–52.5% at $P_c=10$ MPa and $P_w=2$ MPa and decrease by 13.9%–24.5% at $P_c=15$ MPa and $P_w=2$ MPa. In addition, when P_w is constant at 2 MPa, the decrease in the effects of the two fissures on the residual strength of sandstone samples is more remarkable when $L=5$ mm, $\beta=45^\circ$ and $P_w=8$ MPa than under other conditions.

In Fig. 9b, it can be seen that the residual strengths of the double-fissure samples decrease by 24.4%–28.1% at $P_c=15$ MPa and $P_w=5$ MPa and decrease by 20.4%–40.1% at $P_c=15$ MPa and $P_w=8$ MPa compared with the residual strength of the intact samples. Moreover, when P_c is constant at 15 MPa, the decrease in the effects of the two fissures on the residual strength of sandstone samples is more remarkable when $L=5$ mm, $\beta=45^\circ$ and $P_w=8$ MPa than under other conditions.

3.3 Deformation Properties

3.3.1 Elastic Modulus and Possion's Ratio Under Different Confining Pressures

The elastic modulus E and Possion's ratio μ of the tested samples under various confining pressures (5, 10, and 15 MPa) and a constant water pressure of 2 MPa are shown in Fig. 10. The elastic modulus is positively correlated with the confining pressure for all the tested samples. Furthermore, compared with the intact samples, the double-fissure sample E drops by 2.0%–15.3%, 10.6%–12.5% and 1.1%–8.8% under confining pressures of 5, 10 and 15 MPa, respectively. As the confining pressure increases, Possion's ratio of the double-fissure samples with bridge ligaments of $L=5$ mm and $\beta=45^\circ$, $L=10$ mm and $\beta=75^\circ$ and $L=15$ mm and $\beta=45^\circ$ exhibits a nonlinear increase, but it first decreases and then increases when $L=10$ mm and $\beta=45^\circ$, while it exhibits a nonlinear decrease when $L=10$ mm and $\beta=15^\circ$.

3.3.2 Elastic Modulus and Possion's Ratio Under Different Water Pressures

Figure 11 shows the influence of water pressure on the elastic modulus E and Possion's ratio μ of the tested samples. The elastic modulus of the double-fissure samples is negatively correlated with the water pressure. Furthermore, it drops by 5.6%–16.0% and 11.0%–18.4% compared with that of the intact samples underwater pressures of 5 and 8 MPa, respectively. However, Possion's ratio of the double-fissure samples

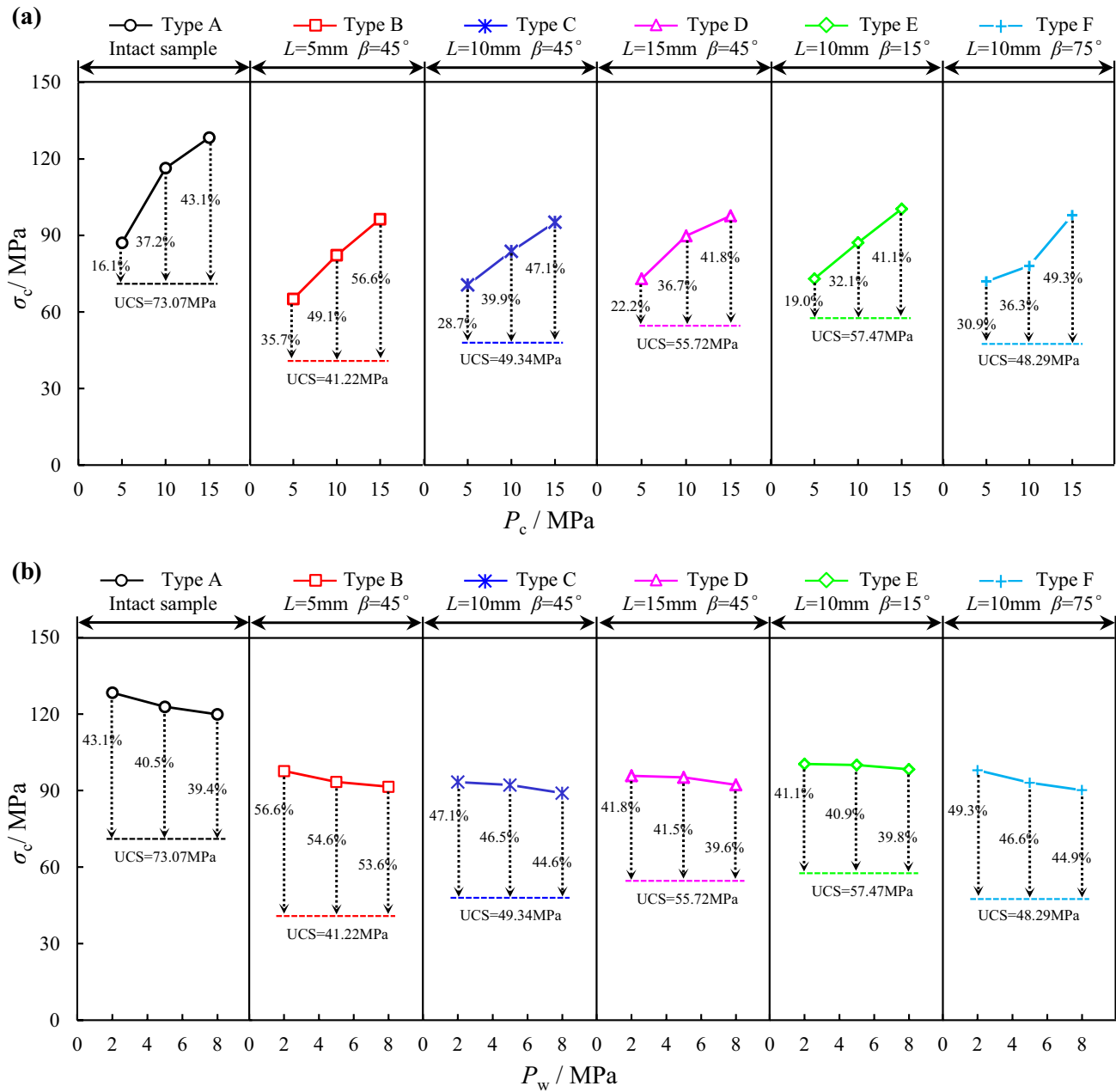


Fig. 8 Peak strength of samples with double fissures

remains approximately 8.3%–38.7% and 25.2%–45.6% higher than that of the intact samples underwater pressures of 5 and 8 MPa, respectively. In addition, μ first decreases and then increases with increasing water pressure from 2 to 8 MPa. Finally, these results show that the influence of the presence of fissures with various bridge ligaments is positively correlated to the water pressure.

3.4 Permeability Evolution Laws

3.4.1 Effect of Confining Pressure on Permeability Evolution Laws

The axial strain-volumetric strain and axial strain-permeability curves of the double-fissure samples with various bridge ligament lengths under a constant water pressure of 2 MPa and different confining pressures of 5, 10, and 15 MPa are shown in Fig. 12. In this figure, each plot can be divided into five segments by the values of k_0 , k_{ci} , k_{cd} , k_c and k_{max} , where

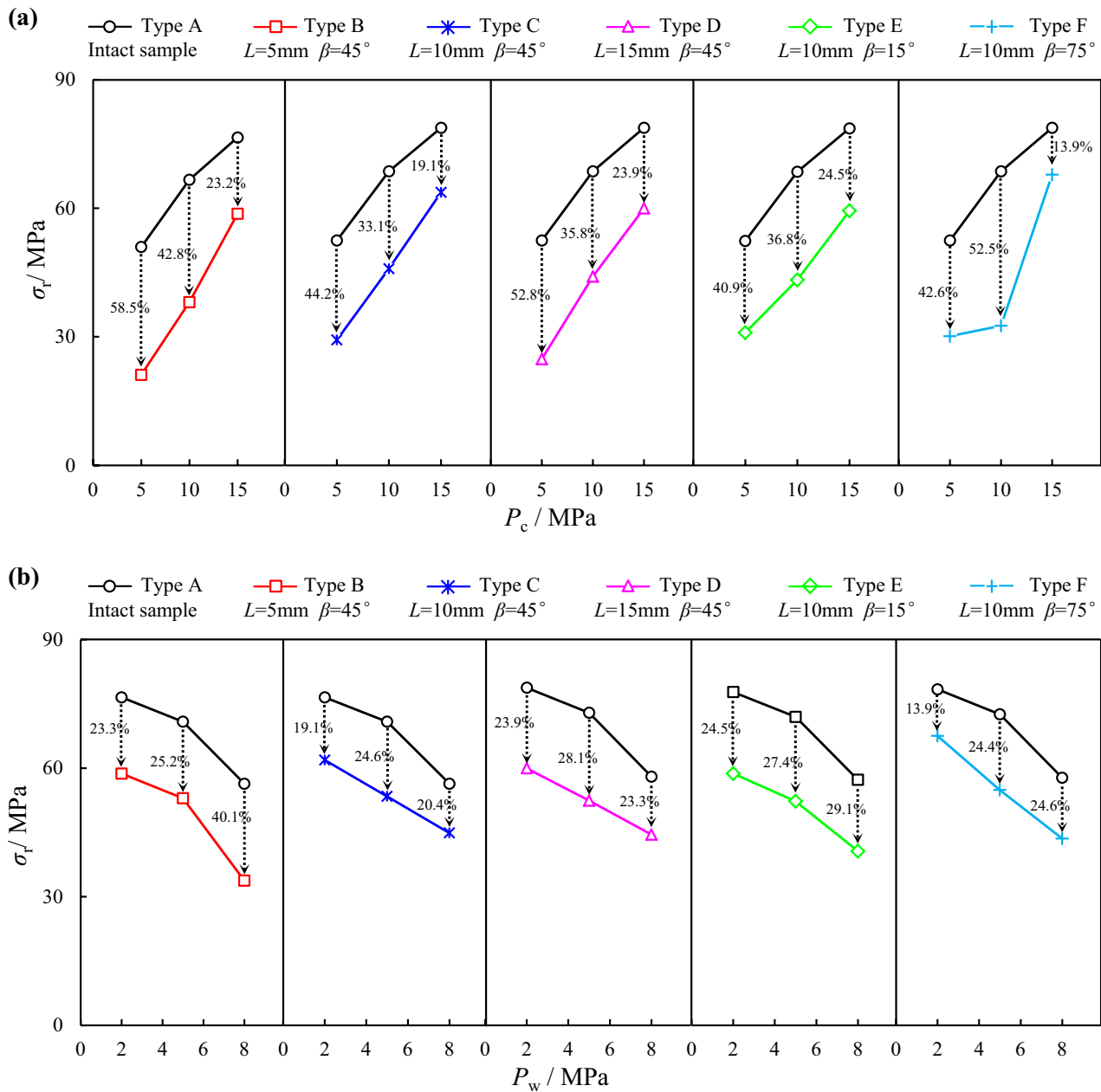


Fig. 9 Residual strength of the tested samples: **a** under different confining pressures and **b** under different water pressures

k_0 denotes the initial permeability, k_{ci} , k_{cd} and k_c denote the permeability corresponding to the crack initiation threshold, macroscale failure threshold and peak strength, respectively, and k_{max} denotes the maximum permeability.

The shape of the axial strain-permeability curves can be described as an approximately “S”-shaped curve. The values of ε_{vc} and ε_v increase, but the permeability decreases steadily, caused by the closure of the primary pores and microcracks, in the segment from k_0 to k_{ci} . Then, ε_{vc} decreases and the permeability increases with a decreasing rate in the segment from k_{ci} to k_{cd} because of the initiation of new

cracks. Furthermore, a decrease in ε_v and a steady increase in the permeability occurs in the segment from k_{cd} to k_c ; meanwhile, macroscale cracks are generated. With a further increase in axial strain, the macroscale cracks reach the top and bottom boundary of the samples, creating a main seepage channel and leading to a sharp increase in permeability to its maximum value k_{max} . Finally, the shearing mechanism of macroscale cracks is enhanced with further axial loading under confining pressure, and the seepage channel is gradually destroyed, which leads to a decrease in permeability after peaking at k_{max} .

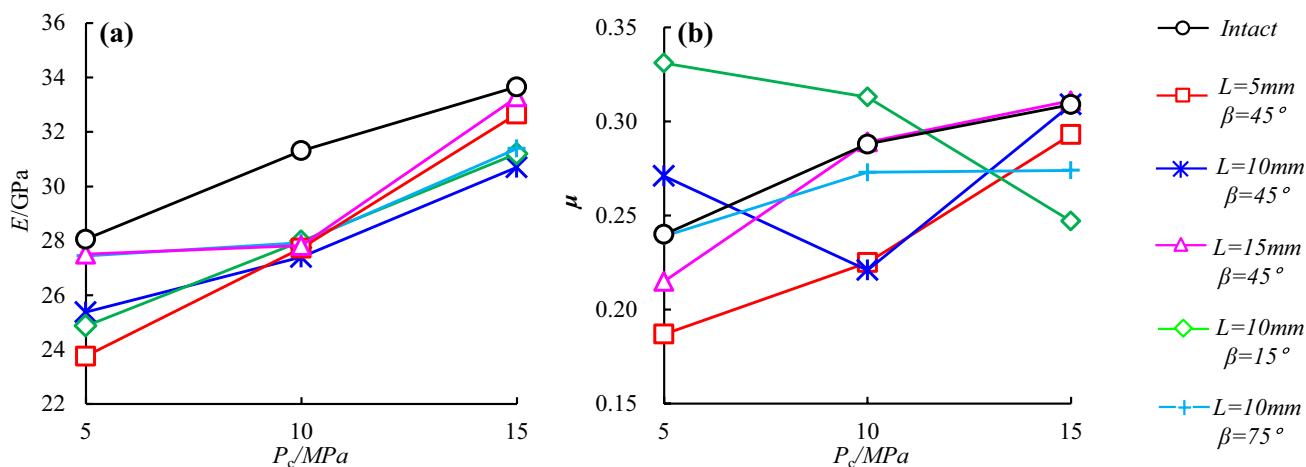


Fig. 10 a Elastic modulus and b Poisson's ratio of the double-fissure sandstone samples under various confining pressures

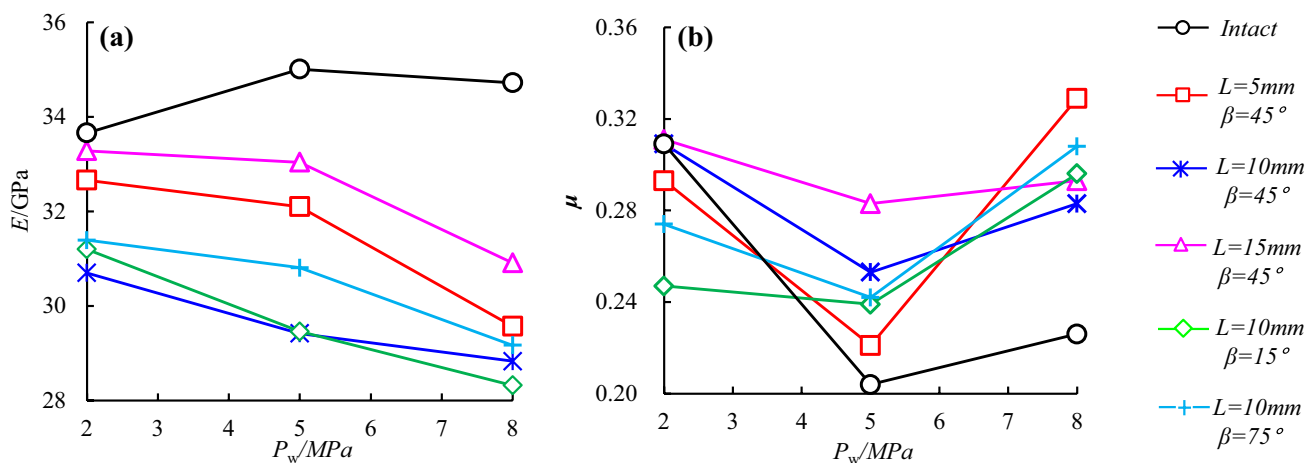


Fig. 11 a Elastic modulus and b Poisson's ratio of the double-fissure sandstone samples under various water pressures

No remarkable changes in the variation patterns of the permeability curves are identifiable before the maximum value is reached, under confining pressures of 5, 10 and 15 MPa. After reaching its maximum value, the permeability decreases with some fluctuation (especially when $L=5, 10\text{ mm}$ and $\beta=45^\circ$) under a confining pressure of 5 MPa due to the propagation of secondary cracks. However, the permeability decreases smoothly to a relatively stable value under higher confining pressures of 10 and 15 MPa.

The influence of the confining pressure, ligament length and bridge angle on k_0-k_c is considerably less than that on k_{max} . Furthermore, the k_{max} of the double-fissure samples with different ligament lengths and bridge angles varies from 87.09×10^{-18} – $112.54 \times 10^{-18}\text{ m}^2$ under a confining pressure of 5 MPa and varies from 46.97×10^{-18} – $68.47 \times 10^{-18}\text{ m}^2$ under a confining pressure of 10 MPa. Finally, k_{max} varies from 27.17×10^{-18} – $35.63 \times 10^{-18}\text{ m}^2$ under a confining

pressure of 15 MPa. It can be concluded that the influence of the ligament length and bridge angle on the permeability under lower confining pressure is greater than that under higher confining pressure.

3.4.2 Effect of Water Pressure on Permeability Evolution Laws

Figure 13 shows the axial strain-volumetric strain and axial strain-permeability curves of the double-fissure samples with various bridge ligaments under a constant confining pressure of 15 MPa and different water pressures of 2, 5 and 8 MPa. There is no considerable deviation in the variation patterns of these permeability curves before the maximum permeabilities are reached under different water pressures.

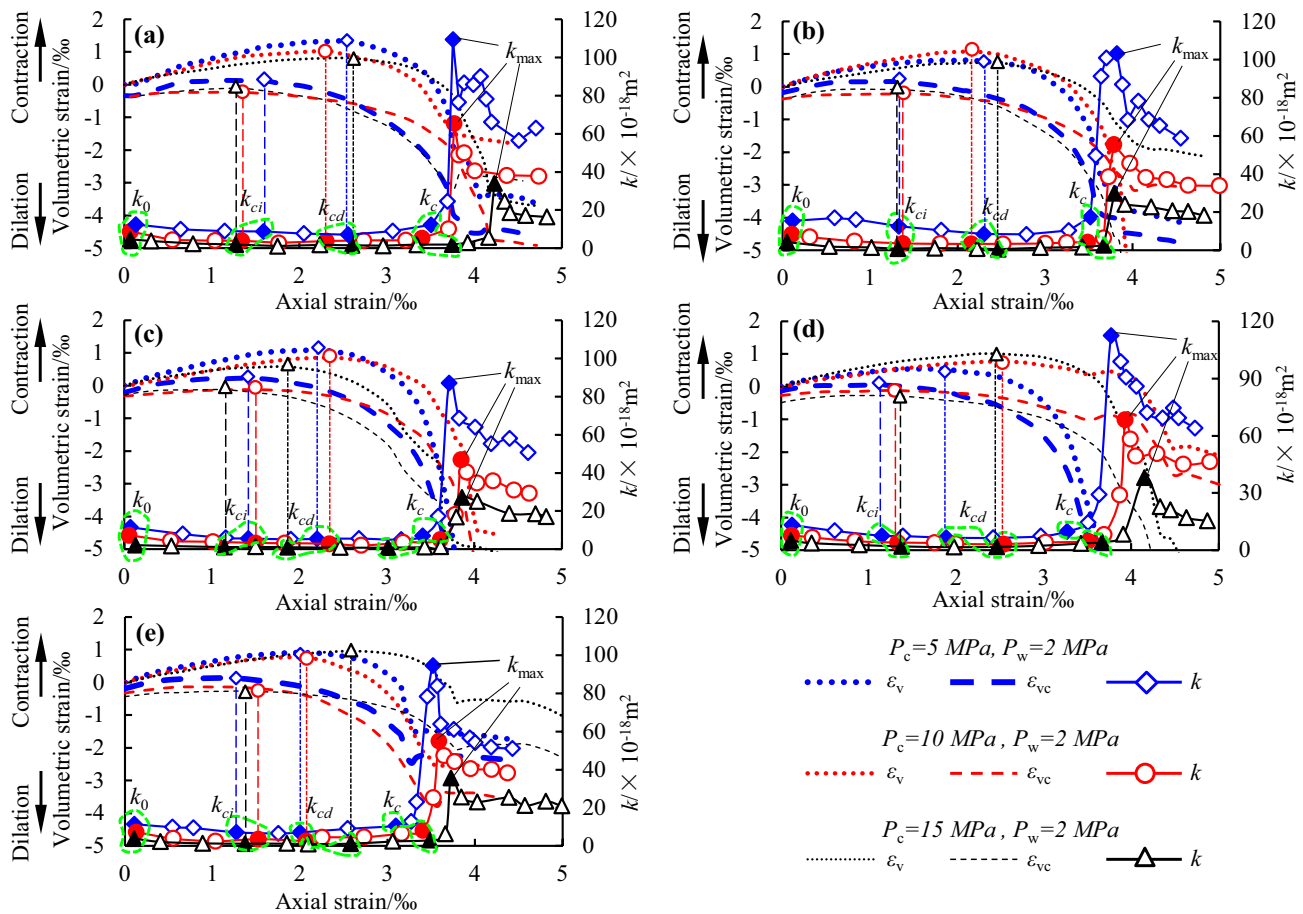


Fig. 12 Permeability evolution laws of double-fissure samples under different confining pressures and the same water pressures: **a** $L=5$ mm and $\beta=45^\circ$; **b** $L=10$ mm and $\beta=45^\circ$; **c** $L=15$ mm and $\beta=45^\circ$; **d** $L=10$ mm and $\beta=15^\circ$; and **e** $L=10$ mm and $\beta=75^\circ$

The permeabilities in the range of k_0 – k_c of the double-fissure samples with different ligament lengths and bridge angles under water pressures of 5 MPa and 8 MPa vary from 2.95×10^{-18} – 7.68×10^{-18} m² and 4.83×10^{-18} – 13.63×10^{-18} m², respectively. Additionally, the values of k_{\max} are in the ranges of 33.71×10^{-18} – 45.28×10^{-18} m² and 64.04×10^{-18} – 77.67×10^{-18} m² under water pressures of 5 and 8 MPa, respectively. Therefore, the influence of the ligament length and bridge angle on permeability is positively correlated with the water pressure.

3.5 Failure Behavior

3.5.1 Description of Failure Modes

The crack types mainly include “wing crack (W)”, “anti-wing crack (AW)” and “secondary crack (SC)” (Park and Bobet 2009; Yang and Jing 2011). The crack coalescence patterns mainly include “no coalescence (NC)”, “direct

coalescence (DC)” and “indirect coalescence (INC)” (Wong and Einstein 2009; Janeiro and Einstein 2010; Morgan et al. 2013). In this study, the failure modes of the double-fissure samples with different bridge ligaments under hydromechanical coupling conditions can be divided into five categories based on the crack types and the crack coalescence patterns, which are shown in Tables 4 and 5.

1. Mode I failure “W + INC”: wing cracks initiate at the outer tips of both preexisting fissures and propagate to the top and bottom boundaries of the sample. Additionally, a wing crack and an anti-wing crack initiate at the two inner tips, respectively, which indirectly coalesce at a point outside the bridge zone.
2. Mode II failure “W + AW + INC”: a wing crack is generated at one of the outer tips of the preexisting fissures, and an anti-wing crack is generated at the other outer tip. Furthermore, indirect coalescence outside the bridge zone occurs.

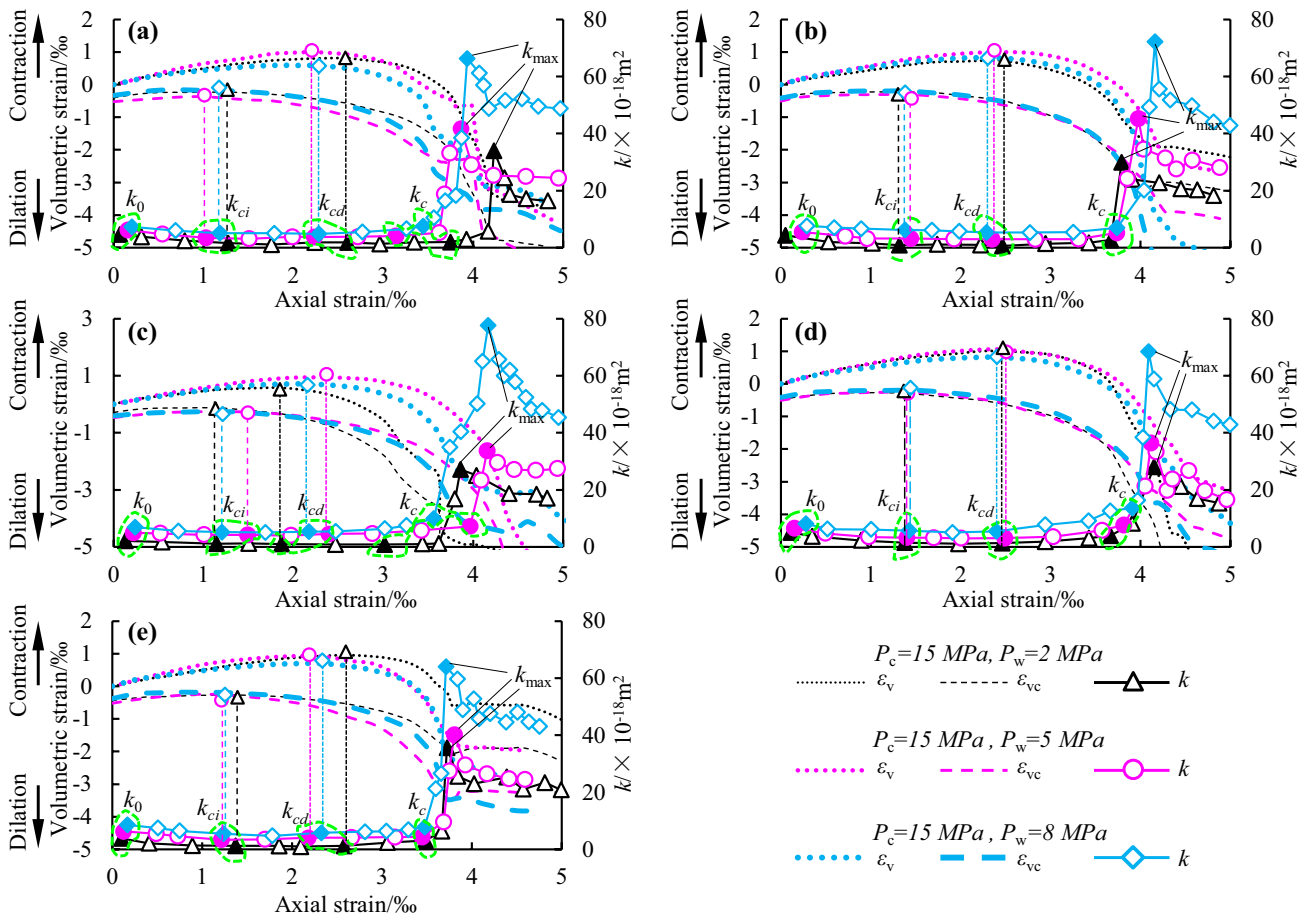


Fig. 13 Permeability evolution laws of the double-fissure samples under the same confining pressure and different water pressures: **a** $L = 5$ mm and $\beta = 45^\circ$; **b** $L = 10$ mm and $\beta = 45^\circ$; **c** $L = 15$ mm and $\beta = 45^\circ$; **d** $L = 10$ mm and $\beta = 15^\circ$; and **e** $L = 10$ mm and $\beta = 75^\circ$

3. Mode III failure “AW + INC”: anti-wing cracks are generated at the outer tips of both preexisting fissures. The cracks that initiate at the inner tips of the preexisting fissures indirectly coalesce at a point outside the bridge zone.
4. Mode IV failure “AW + NC”: anti-wing cracks are generated at all outer and inner tips of the preexisting fissures, but no coalescence occurs between the preexisting fissures.
5. Mode failure V “W + DC”: two wing cracks are initiated at the outer tips of the preexisting fissures and then expand to the top and bottom of the tested samples. Moreover, a shear crack directly coalesces with the two preexisting fissures in the bridge zone.

3.5.2 Effect of Confining Pressure on Failure Behavior

Table 4 shows that, at a confining pressure of 5 MPa, the failure of double-fissure samples with a lower ligament length and a moderate bridge angle ($L = 5$ mm and $\beta = 45^\circ$) is mode I, which changes to mode II as the ligament length

increases to 10 mm and 15 mm. Additionally, the failure of the tested samples changed to mode III and mode V for a lower bridge angle of 15° and a higher bridge angle of 75° . As the confining pressure increases from 5 to 10 MPa, the failure of the tested samples with $L = 15$ mm and $\beta = 45^\circ$ and $L = 10$ mm and $\beta = 15^\circ$ change to mode III and mode IV, respectively, but no clear changes were observed for the tested samples with $L = 5$ mm and $\beta = 45^\circ$, $L = 10$ mm and $\beta = 45^\circ$ and $L = 10$ mm and $\beta = 75^\circ$. As the confining pressure increases from 10 to 15 MPa, the failures of the tested samples with $L = 5$ mm and $\beta = 45^\circ$ and $L = 10$ mm and $\beta = 45^\circ$ change to mode II and III, respectively; moreover, the failure mode remains unchanged in the samples with the other tested bridge ligaments.

The above analysis shows that the confining pressures have a great influence on the failure modes of the double-fissure samples with a bridge angle that is not higher than the fissure angle. The propagation of wing cracks and the coalescence of cracks between the two preexisting fissures are inhibited by an increase in the confining pressure and

Table 4 Failure modes of double-fissure samples under different confining pressures and the same water pressures

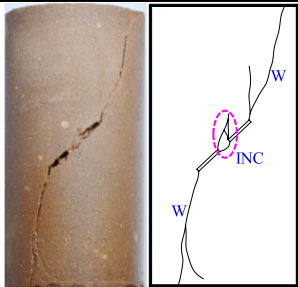
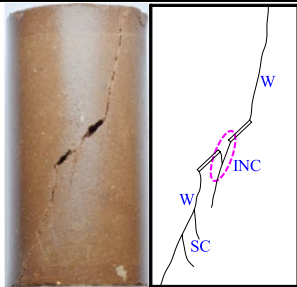
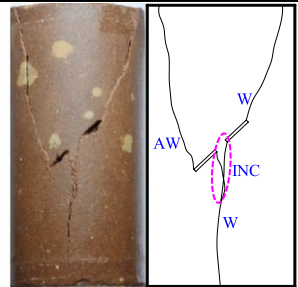
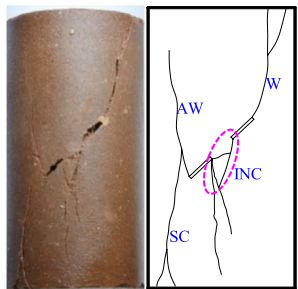
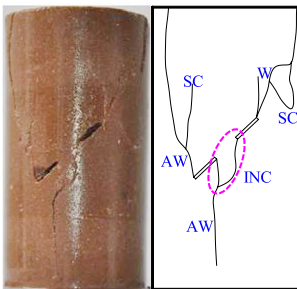
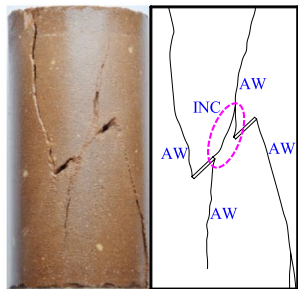
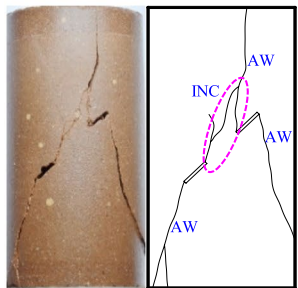
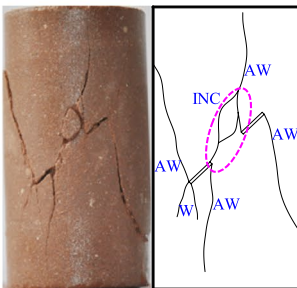
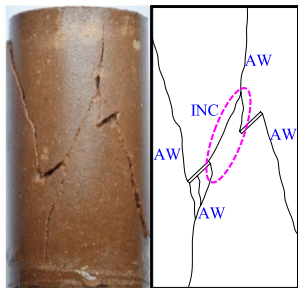
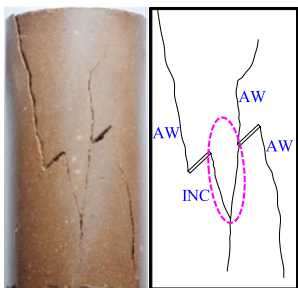
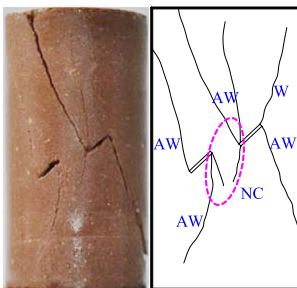
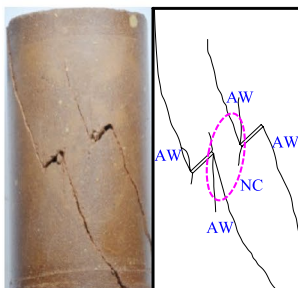
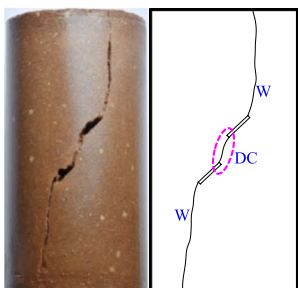
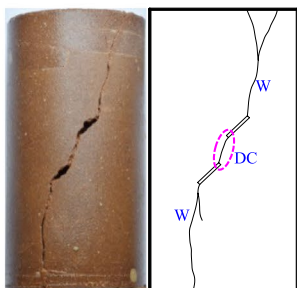
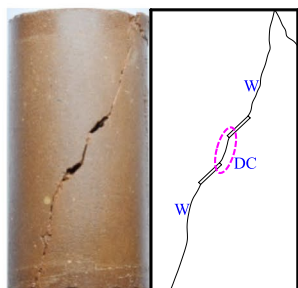
	$P_c=5\text{ MPa } P_w=2\text{ MPa}$	$P_c=10\text{ MPa } P_w=2\text{ MPa}$	$P_c=15\text{ MPa } P_w=2\text{ MPa}$
$L=5\text{ mm}$ $\beta=45^\circ$	 <p>Mode I</p>	 <p>Mode I</p>	 <p>Mode II</p>
$L=10\text{ mm}$ $\beta=45^\circ$	 <p>Mode II</p>	 <p>Mode II</p>	 <p>Mode III</p>
$L=15\text{ mm}$ $\beta=45^\circ$	 <p>Mode II</p>	 <p>Mode III</p>	 <p>Mode III</p>
$L=10\text{ mm}$ $\beta=15^\circ$	 <p>Mode III</p>	 <p>Mode IV</p>	 <p>Mode IV</p>
$L=10\text{ mm}$ $\beta=75^\circ$	 <p>Mode V</p>	 <p>Mode V</p>	 <p>Mode V</p>

Table 4 (continued)

P_c confining pressure, P_w water pressure, W wing crack, AW anti-wing crack, INC indirect coalescence, SC secondary crack, NC no coalescence, DC direct coalescence

ligament length as well as a decrease in the bridge angle due to a more predominant shear failure mode.

3.5.3 Effect of Water Pressure on Failure Behavior

In Table 5, as the water pressure increases from 2 to 5 MPa, the failure modes of the double-fissure samples with $L=5$ mm and $\beta=45^\circ$, $L=10$ mm and $\beta=45^\circ$ and $L=10$ mm and $\beta=15^\circ$ change from mode II, mode II and mode IV to type I, mode III and mode II, respectively. Furthermore, as the water pressure increases from 5 to 8 MPa, no remarkable changes in the failure modes of the tested samples are observed, except that the number and length of wing cracks slightly increase.

Therefore, it can be concluded that the water pressure has a great influence on the failure modes of the double-fissure samples with a ligament that is not longer than the fissure length and with a low bridge angle. Additionally, the expansion of wing cracks and the coalescence of cracks between the two preexisting fissures are promoted by the increase in water pressure and bridge angle.

Moreover, the results indicate that the relative effects of the four factors on the failure modes of double-fissure samples, from the greatest effect to the least effect, are as follows: bridge angle, ligament length, confining pressure and water pressure.

3.5.4 Internal Crack Behavior

Figures 14, 15, 16, 17 and 18 show the post-test vertical cross sections, horizontal slices and three-dimensional images of the double-fissure sandstone samples under a confining pressure of 10 MPa coupled with a water pressure of 2 MPa. All five typical crack coalescence types are represented in these samples.

When $L=5$ mm and $\beta=45^\circ$, the failure is mode I, as shown in Fig. 14. Additionally, the internal crack coalescence pattern in the rock bridge zone between the “H₁–H₁” and “H₂–H₂” sections approximately matches the surface pattern, transforming from indirect coalescence to direct coalescence between the “H₃–H₃” and “H₄–H₄” sections.

When $L=10$ mm and $\beta=45^\circ$, the failure is mode II, as shown in Fig. 15. Furthermore, the orientation of the internal cracks that converge near the rock bridge region is aligned with the load direction.

When $L=15$ mm and $\beta=45^\circ$, the failure is mode III, as shown in Fig. 16. Moreover, the convergence point of

internal cracks near the rock bridge region in the “H₁–H₁” and “H₄–H₄” sections appears later than that in the “H₂–H₂” and “H₃–H₃” sections, which indicates that the cracks on the surface of the samples more easily expand than those deeper within the samples.

When $L=10$ mm and $\beta=15^\circ$, the failure is mode IV, as shown in Fig. 17. Furthermore, there are no remarkable differences between the main cracks inside and on the surface of the tested sample. The lengths of the secondary cracks inside the sample are shorter than those observed on the surface of the sample.

When $L=10$ mm and $\beta=75^\circ$, the failure is mode V, as shown in Fig. 18. Additionally, only slight changes in the crack expanding paths and coalescence types are observed inside the samples.

In addition, the wing cracks and anti-wing cracks that initiate at the outer tips of preexisting fissures are observed as a curved surface inside the samples, especially for failure modes II, III and IV. Furthermore, the width of cracks near the boundaries of the samples is generally greater than that in other regions.

4 Discussion

Previous experimental studies have mainly focused on the mechanical and failure behaviors of fissured samples under uniaxial and triaxial compression or the hydromechanical behavior of intact samples. Compared with these previous studies, there are some novel findings in this paper. The results of hydromechanical coupling tests on sandstone with two fissures are summarized in Figs. 19, 20, and 21 as well as Table 6.

1. The failure of a double-fissure sample changes from mode I to mode II with the increase of P_c and the decrease of P_w when $L=5$ mm and $\beta=45^\circ$. Additionally, it changes from mode II to mode III with the increase of P_c and the decrease of P_w when $L=10$ mm and $\beta=45^\circ$. The failure of the tested sample with $L=15$ mm and $\beta=15^\circ$ is always mode III despite changes in P_w , and it changes from mode II to mode III with the increase of P_c . Furthermore, the failure of the tested sample changes from mode III to mode IV with the increase of P_c when $L=10$ mm and $\beta=15^\circ$, and it changes from mode IV to mode II. Moreover, it is always mode V despite changes in P_c and P_w when $L=10$ mm and $\beta=75^\circ$. In addition, the effects of the ligament length and bridge angle on the

Table 5 Failure modes of double-fissure samples under the same confining pressure and different water pressures

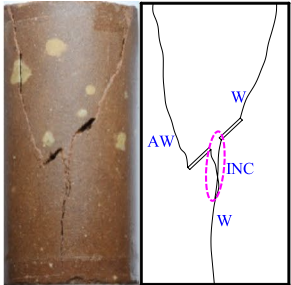
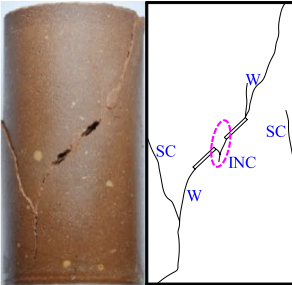
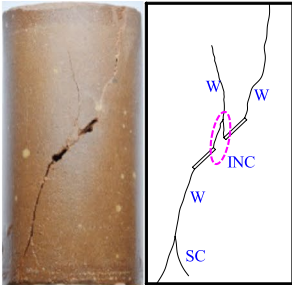
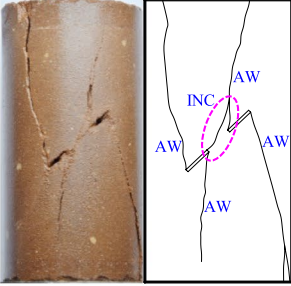
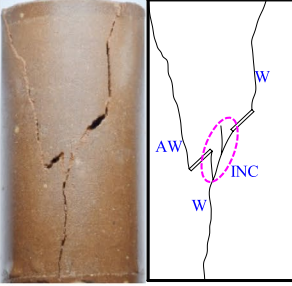
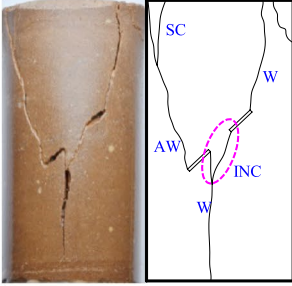
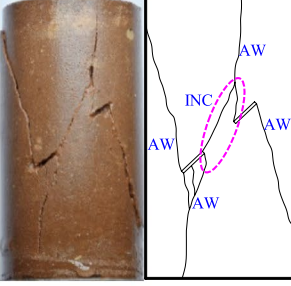
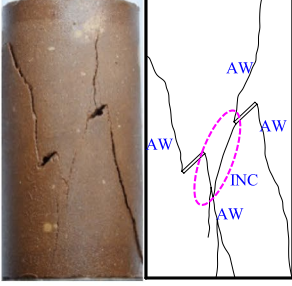
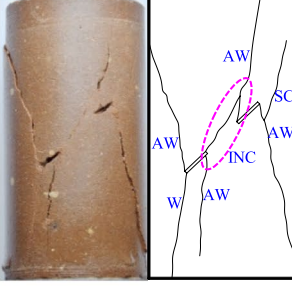
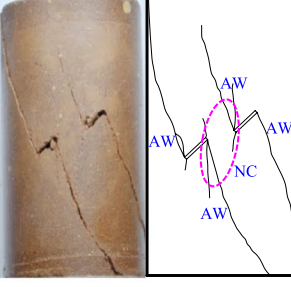
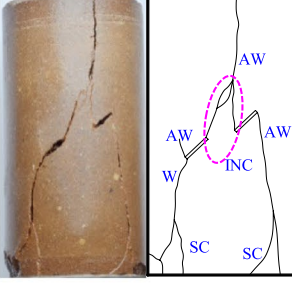
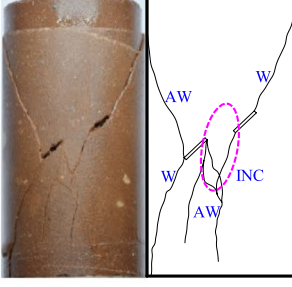
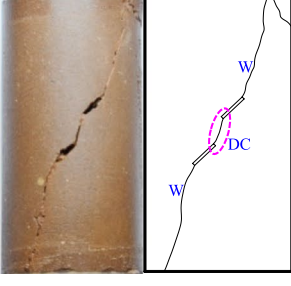
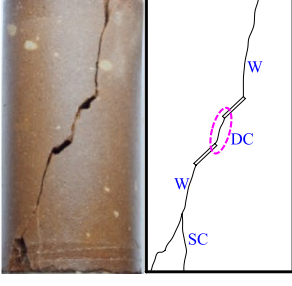
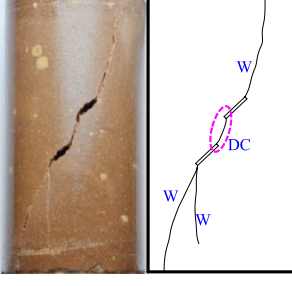
	$P_c=15\text{ MPa } P_w=2\text{ MPa}$	$P_c=15\text{ MPa } P_w=5\text{ MPa}$	$P_c=15\text{ MPa } P_w=8\text{ MPa}$
$L=5\text{ mm}$ $\beta=45^\circ$			
	Mode II	Mode I	Mode I
$L=10\text{ mm}$ $\beta=45^\circ$			
	Mode III	Mode II	Mode II
$L=15\text{ mm}$ $\beta=45^\circ$			
	Mode III	Mode III	Mode III
$L=10\text{ mm}$ $\beta=15^\circ$			
	Mode IV	Mode II	Mode II
$L=10\text{ mm}$ $\beta=75^\circ$			
	Mode V	Mode V	Mode V

Table 5 (continued)

P_c confining pressure, P_w water pressure, W wing crack, AW anti-wing crack, INC indirect coalescence, SC secondary crack, NC no coalescence, DC direct coalescence

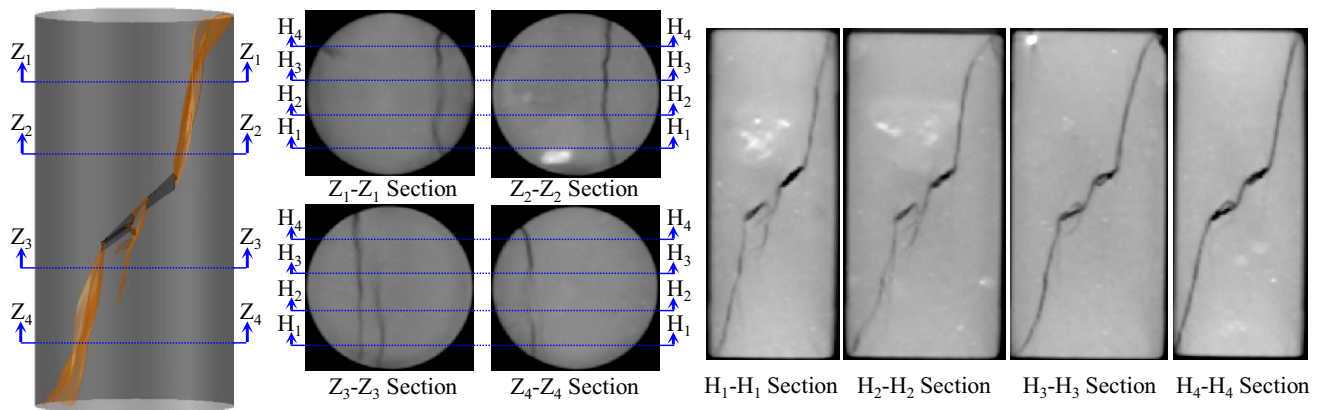


Fig. 14 CT images of the double-fissure sample with $L=5\text{ mm}$ and $\beta=45^\circ$

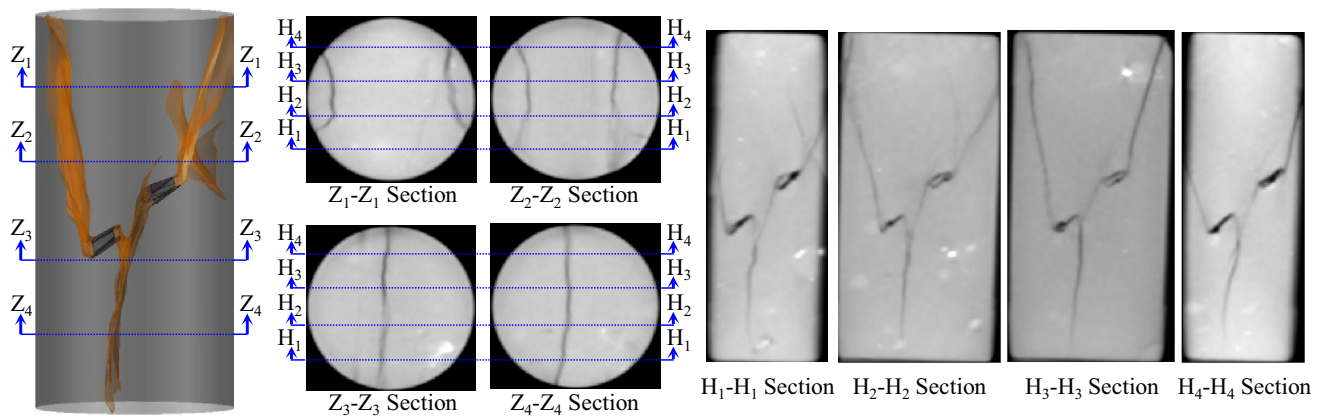


Fig. 15 CT images of the double-fissure sample with $L=10\text{ mm}$ and $\beta=45^\circ$

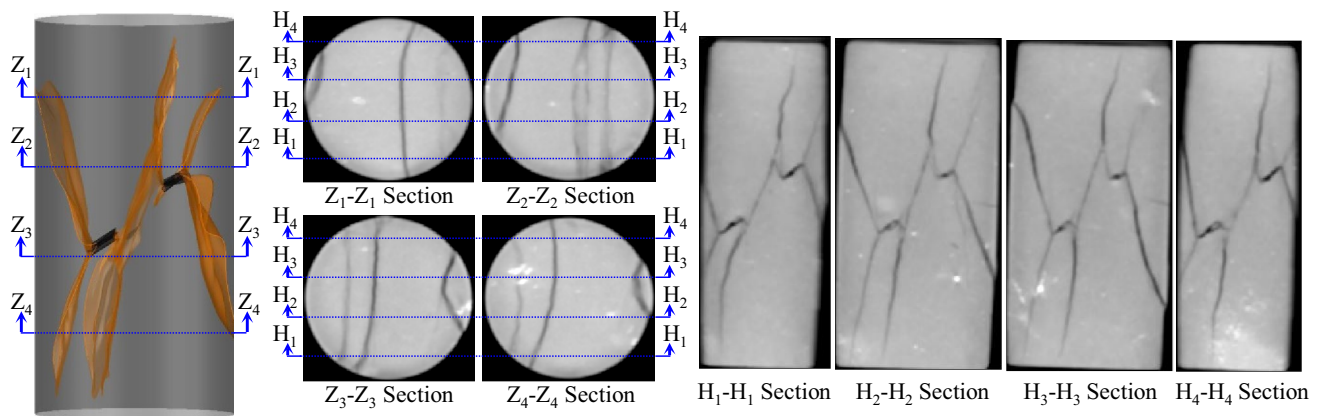


Fig. 16 CT images of the double-fissure sample with $L=15\text{ mm}$ and $\beta=45^\circ$

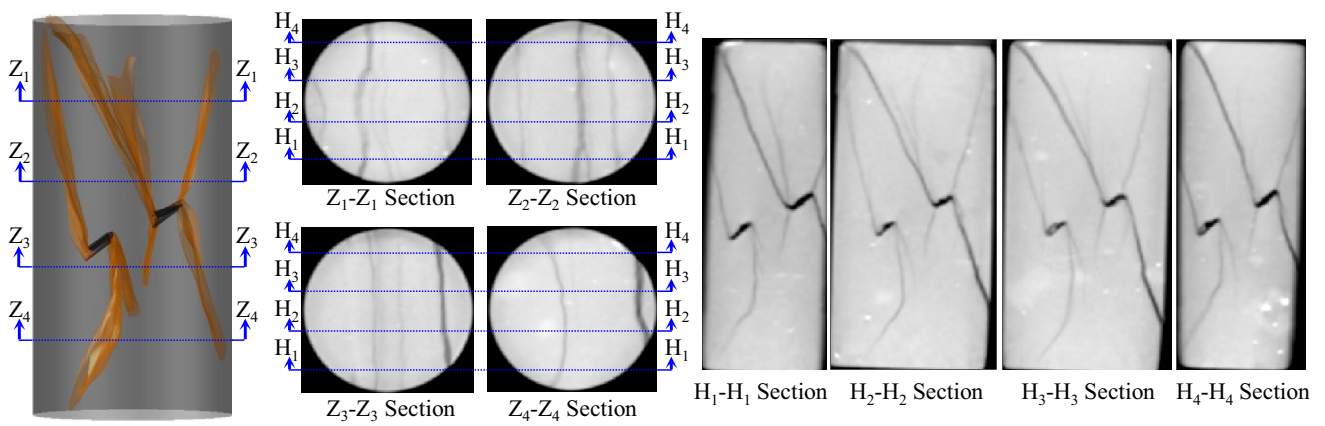


Fig. 17 CT images of the double-fissure sample with $L=10$ mm and $\beta=15^\circ$

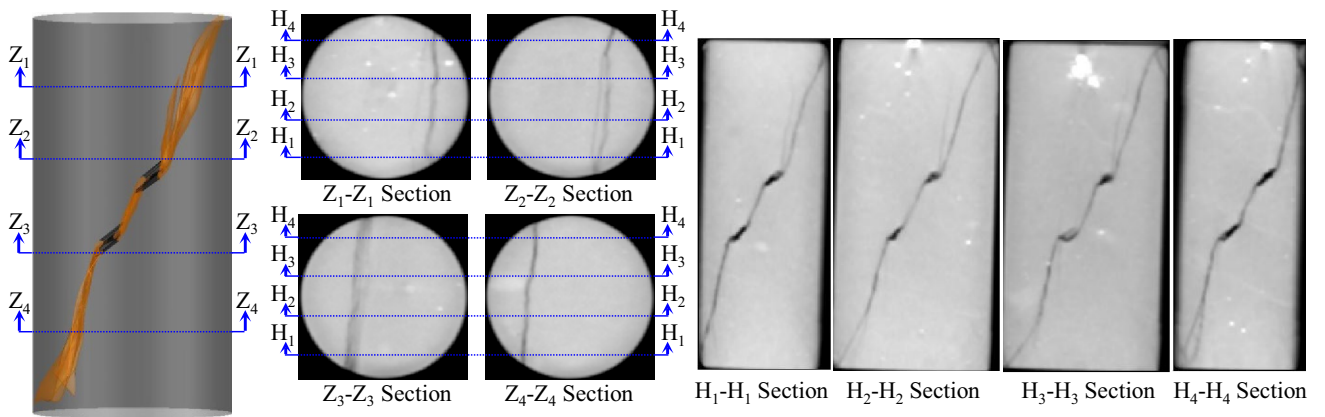
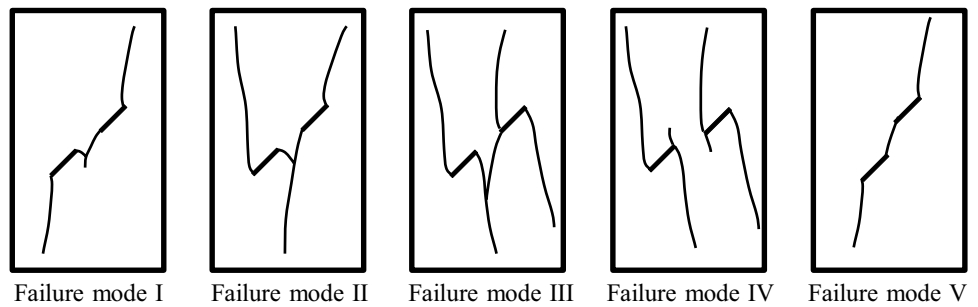


Fig. 18 CT images of the double-fissure sample with $L=10$ mm and $\beta=75^\circ$

Fig. 19 Schematic diagrams of the five failure types



failure modes of double-fissures sandstone are greater than those of the confining pressure and water pressure.

- The values of σ_{ci} , σ_{cd} and σ_c of tested sandstone samples all increase with increasing P_c and decrease with decreasing P_w , as shown in Fig. 20, which are similar to the previous studies (Huang et al. 2016a, 2019; Wang et al. 2014a, 2016b). The minimum values of them are all under $P_c=5$ MPa and $P_w=2$ MPa in this paper. Furthermore, the novel finding is that the minimum values of σ_{ci} , σ_{cd} and σ_c are not found in the same sample. The

σ_{ci} and σ_c are minimum when $L=5$ mm and $\beta=45^\circ$, and the σ_{cd} is minimum when $L=10$ mm and $\beta=15^\circ$, while the σ_c is minimum when $L=5$ mm and $\beta=45^\circ$. These results indicate that the values of σ_{ci} and σ_c are more sensitive to ligament length, but the effect of the bridge angle is greater than that of ligament length on the value of σ_{cd} .

- The permeabilities of tested sandstone samples all increase with decreasing P_c and increasing P_w values, as shown in Fig. 21, which are similar to the

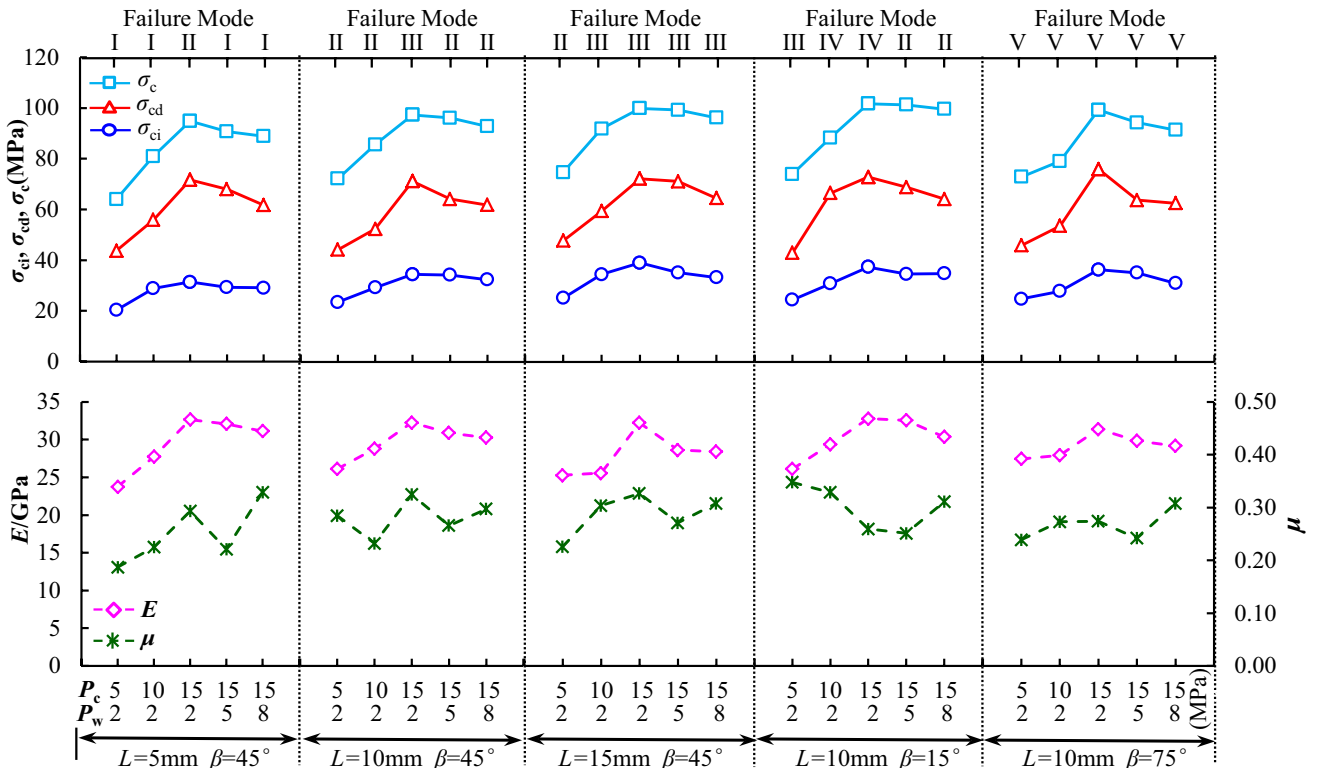


Fig. 20 Strength and deformation parameters of double-fissure samples with different failure modes

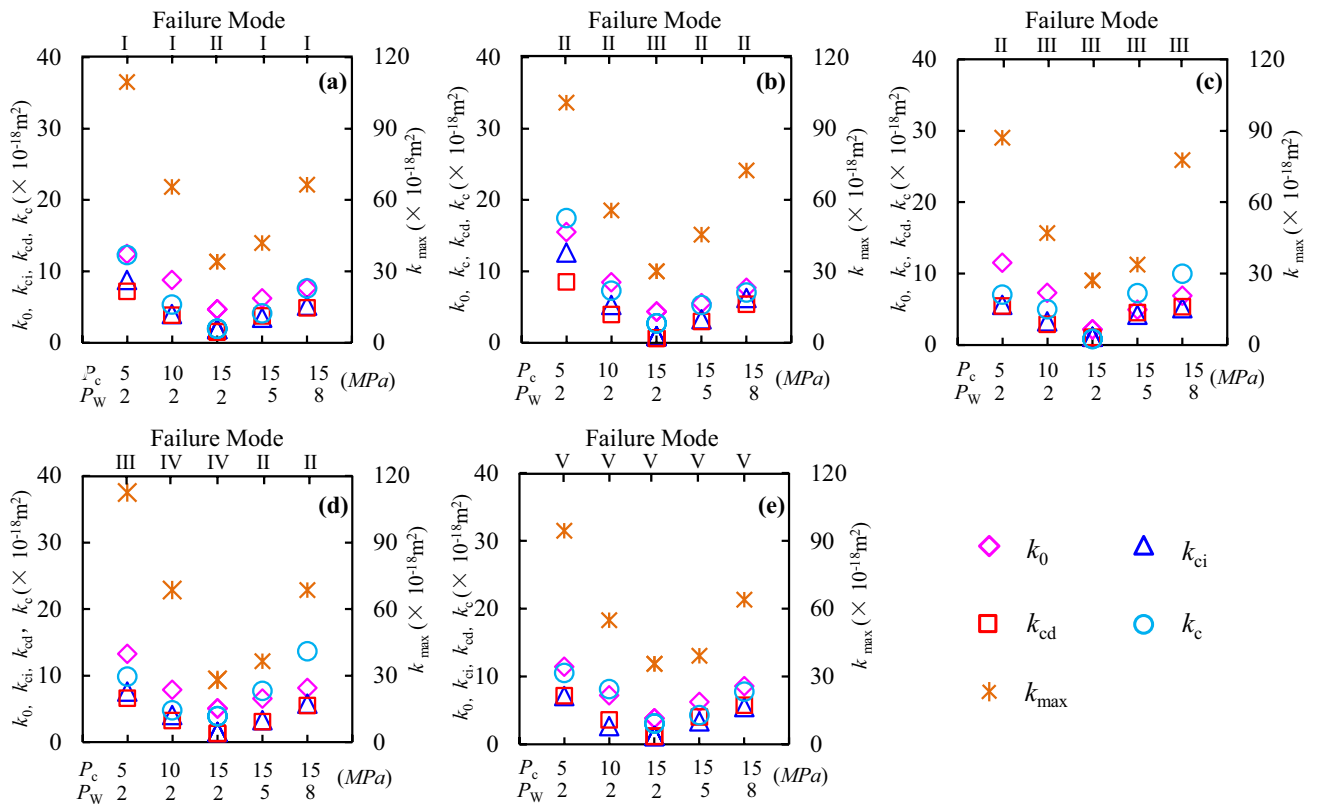


Fig. 21 Permeability of double-fissure samples with different failure modes: a $L=5$ mm and $\beta=45^\circ$; b $L=10$ mm and $\beta=45^\circ$; c $L=15$ mm and $\beta=45^\circ$; d $L=10$ mm and $\beta=15^\circ$; and e $L=10$ mm and $\beta=75^\circ$

Table 6 Strength, deformation and permeability properties of tested samples corresponding to various failure modes

P_c	P_w	L (mm)	B (°)	σ (MPa)			E (GPa)	μ	k (10^{-18}) m^2			Failure mode		
				σ_{ci}	σ_{cd}	σ_c			k_0	k_{ci}	k_{cd}		k_c	k_{max}
5	2	5	45	20.35	43.74	64.09	23.76	0.187	12.38	8.76	7.15	12.25	109.37	I
5	2	10	45	22.58	42.38	69.24	25.38	0.271	15.47	12.58	8.49	17.44	100.87	II
5	2	15	45	24.13	45.79	71.58	27.51	0.331	11.50	5.62	5.44	7.04	87.09	II
5	2	10	15	23.46	41.47	70.94	24.87	0.331	13.27	7.61	6.62	9.84	112.54	III
5	2	10	75	23.79	43.98	69.92	27.45	0.239	11.45	7.11	7.17	10.53	94.55	V
10	2	5	45	28.86	55.91	80.97	27.73	0.225	8.71	3.97	3.80	5.30	65.40	I
10	2	10	45	28.07	50.21	82.12	27.40	0.221	8.42	5.25	3.91	7.26	55.44	II
10	2	15	45	33.03	56.95	88.08	27.82	0.289	7.32	3.31	2.87	5.00	46.97	III
10	2	10	15	29.59	63.74	84.68	27.98	0.313	7.89	4.05	3.24	4.80	68.47	IV
10	2	10	75	26.69	51.35	75.83	27.93	0.273	7.25	2.70	3.59	8.15	54.99	V
15	2	5	45	31.35	71.69	94.88	32.66	0.293	4.62	1.86	1.51	1.92	33.98	II
15	2	10	45	33.06	68.28	93.32	30.70	0.309	4.31	0.87	0.57	2.66	29.52	III
15	2	15	45	37.38	69.23	95.77	35.06	0.311	2.14	1.12	1.03	0.82	27.17	III
15	2	10	15	35.82	69.82	97.55	31.20	0.247	5.05	1.53	1.31	3.92	28.08	IV
15	2	10	75	34.80	72.84	95.16	31.39	0.274	3.84	1.21	1.17	3.07	35.63	V
15	5	5	45	29.29	65.09	90.91	32.10	0.221	6.17	3.43	3.69	4.05	41.74	I
15	5	10	45	32.87	61.50	92.17	29.42	0.253	5.51	3.23	2.95	5.23	45.28	II
15	5	15	45	33.72	68.17	95.16	31.15	0.258	4.91	4.22	4.53	7.25	33.71	III
15	5	10	15	33.16	66.05	97.17	31.01	0.239	6.53	3.27	3.06	7.68	36.49	II
15	5	10	75	33.63	61.08	90.39	29.85	0.242	6.27	3.39	4.04	4.34	39.20	V
15	8	5	45	29.08	61.09	88.90	31.13	0.329	7.59	5.12	4.83	7.54	66.30	I
15	8	10	45	31.06	59.24	88.99	29.78	0.283	7.64	6.24	5.35	6.97	72.21	II
15	8	15	45	31.87	61.89	92.23	30.91	0.293	6.91	5.16	5.36	9.95	77.67	III
15	8	10	15	33.42	61.53	95.52	28.92	0.296	8.15	5.76	5.50	13.63	68.48	II
15	8	10	75	29.70	59.96	87.58	29.17	0.308	8.60	5.51	5.76	7.78	64.04	V

results found in previous studies (Wang et al. 2014a, 2016b; Zhao et al. 2017). Additionally, the novel finding is that the failure modes have a remarkable influence on the permeability evolution laws. The order of $k_{cd} < k_{ci} < k_c < k_0 < k_{max}$ is observed in all failure modes. However, the orders of $k_{cd} < k_{ci} < k_0 < k_c < k_{max}$ and $k_{ci} < k_{cd} < k_c < k_0 < k_{max}$ are also observed in the samples with mode II, III and V failure. Furthermore, the effects of the ligament length and bridge angle on the permeability under lower P_c and higher P_w are greater than that those under higher P_c and lower P_w .

4. The mechanical and permeability characteristics of double-fissure samples under hydromechanical coupling conditions are associated with the failure mode. Furthermore, the strength parameters of samples that exhibit failure mode I are generally lower than those that exhibit other failure modes. In addition, the order of the mechanical and permeability properties affected by failure modes, from greatest to least, is as follows: crack initiation threshold, peak strength, crack damage threshold, elastic modulus, Poisson's ratio and permeability.

5 Conclusions

Unlike previous studies, this paper conducts a series of coupled hydromechanical tests on sandstone samples containing two parallel fissures to fully explore the influence of confining pressure, water pressure and different ligament lengths and bridge angles on the hydromechanical behavior of double-fissure sandstone. The main findings that are different from those of previous studies can be summarized as follows:

(1) Compared with the intact samples, the stress–strain curves of double-fissure samples under hydromechanical coupling conditions fluctuate more after the peak strength, especially when the ligament length and bridge angle are less than those of the fissures.

(2) The ratios of σ_{ci}/σ_c and σ_{cd}/σ_c decrease remarkably with the increase in water pressure, which indicates that the initiation and propagation of cracks are promoted by greater water pressure. Additionally, the peak strength increases by 34.8%–47.4% as the confining pressure increases by two times. However, the peak strength decreases by 2.1%–8.0% as the water pressure increases by three times. Therefore, the influence of confining pressure is greater than that of water pressure on the peak strength. Compared with σ_{ci}/σ_c and E of the intact samples, σ_{ci}/σ_c and E of the double-fissure samples decrease by 13.3%–31.8% and 2.4%–12.2%, respectively. However, μ increases by 8.3%–45.6% underwater pressures of 5 MPa and 8 MPa, indicating that the interaction of crack

propagation and water pressure greatly reduces the strength parameters and accelerates the failure of rocks.

(3) Unlike in the intact samples, in the double-fissure samples under hydromechanical coupling conditions, five failure modes are observed. Additionally, mode I and mode II failure are generally more common in samples with a small ligament length and a small bridge angle. As the ligament length and confining pressure increase and the bridge angle and water pressure decrease, the propagation of wing cracks and crack coalescence are restricted, causing the failure to evolve into mode II and mode III. However, when the bridge angle is higher than the fissure angle, only mode V failure is generated. This indicates that the influence of the bridge angle is greater than that of confining pressure, water pressure and ligament length. Furthermore, the expansion of cracks inside the samples is more restricted than that on the surface of the samples, especially near the rock bridge region.

(4) The failure modes have a great influence on the permeability evolution laws. The order of $k_{cd} < k_{ci} < k_c < k_0 < k_{max}$ is observed in the samples with all types of failure. However, the orders of $k_{cd} < k_{ci} < k_0 < k_c < k_{max}$ and $k_{ci} < k_{cd} < k_c < k_0 < k_{max}$ are also observed in the samples with modes II, III and V failure. Additionally, the influence of the ligament length and bridge angle on the permeability is negatively correlated with the confining pressure but is positively correlated with the water pressure.

(5) The mechanical and permeability properties affected by failure modes, from greatest to least, are as follows: crack initiation threshold, peak strength, crack damage threshold, elastic modulus, Poisson's ratio and permeability.

(6) A greater water pressure promotes the initiation and expansion of cracks. Furthermore, the coupling of crack propagation and water pressure accelerates the fracture of rocks. In addition, the coupling of confining pressure, water pressure and preexisting fissures greatly affects the failure behavior of a rock mass. In particular, when the fissures are coplanar and the ligament length is less than half of the fissure length, the strength parameters of the fractured rock are lower and the corresponding permeability is higher. The reduction in confining pressure and the increase in water pressure further weaken the strength parameters and enhance the permeability. This research can provide useful information for the analysis of the stability of rock engineering involving jointed rocks.

Acknowledgements This study was supported by the National Natural Science Foundation of China (Nos. 41772299, 51279096) and the Open Fund Research Project of State Key Laboratory Breeding Base for Mining Disaster Prevention and Control, China (No. MDPC201815).

Compliance with Ethical Standards

Conflict of interest The authors declare no conflicts of interest.

References

- Afolagboye LO, He JM, Wang SJ (2018) Crack initiation and coalescence behavior of two non-parallel flaws. *Geotech Geol Eng* 36(1):105–133
- Bahaaddini M, Sharrock G, Hebblewhite BK (2013) Numerical investigation of the effect of joint geometrical parameters on the mechanical properties of a non-persistent jointed rock mass under uniaxial compression. *Comput Geotech* 49:206–225
- Bieniawski ZT (1967) Mechanism of brittle fracture of rock: part I—theory of the fracture process. *Int J Rock Mech Min Sci Geomech Abstr* 4(4):395–406
- Brace WF, Walsh JB, Frangos WT (1968) Permeability of granite under high pressure. *J Geophys Res* 73(6):2225–2236
- Cai M, Kaiser PK, Tasaka Y, Maejima T, Morioka H, Mianami M (2004) Generalized crack initiation and crack damage stress thresholds of brittle rock masses near underground excavations. *Int J Rock Mech Min Sci* 41(5):833–847
- Cai YY, Chen X, Yu J, Zhou JF (2018) Numerical study on the evolution of mesoscopic properties and permeability in sandstone under hydromechanical coupling conditions involving industrial internet of things. *IEEE Access* 6:11804–11815
- Cao P, Liu TY, Pu CZ, Lin H (2015) Crack propagation and coalescence of brittle rock-like specimens with pre-existing cracks in compression. *Eng Geol* 187:113–121
- Chen YL (2016) Experimental study of the stress dependence of the permeability of rock. *Geotech Geol Eng* 34(5):1571–1575
- Chen X, Yu J, Tang CA, Li H, Wang SY (2017) Experimental and numerical investigation of permeability evolution with damage of sandstone under triaxial compression. *Rock Mech Rock Eng* 50(6):1529–1549
- Chen X, Tang CA, Yu J, Zhou JF, Cai YY (2018) Experimental investigation on deformation characteristics and permeability evolution of rock under confining pressure unloading conditions. *J Cent South Univ* 25(8):1987–2001
- Davy CA, Skoczylas F, Barnichon JD et al (2007) Permeability of macro-cracked argillite under confinement: gas and water testing. *Phys Chem Earth* 32(8–14):667–680
- Eberhardt E, Stimpson B, Read RS, Stead D (1998) Identifying crack initiation and propagation thresholds in brittle rock. *Can Geotech J* 35(2):222–233
- Fu JW, Chen K, Zhu WS, Zhang XH, Li XJ (2016) Progressive failure of new modelling material with a single internal crack under biaxial compression and the 3-D numerical simulation. *Eng Fract Mech* 165:140–152
- Fu JW, Zhang XH, Zhu WS, Chen K, Guan JF (2017) Simulating progressive failure in brittle jointed rock masses using a modified elastic-brittle model and the application. *Eng Fract Mech* 178:212–230
- Haeri H, Shahriar K, Marji MF, Moarefvand P (2014) Cracks coalescence mechanism and cracks propagation paths in rock-like specimens containing pre-existing random cracks under compression. *J Cent South Univ* 21(6):2404–2414
- Huang D, Gu DM, Yang C, Huang RQ, Fu GY (2016a) Investigation on mechanical behaviors of sandstone with two preexisting flaws under triaxial compression. *Rock Mech Rock Eng* 49:375–399
- Huang YH, Yang SQ, Zhao J (2016b) Three-dimensional numerical simulation on triaxial failure mechanical behavior of rock-like specimen containing two unparallel fissures. *Rock Mech Rock Eng* 49(12):4711–4729
- Huang YH, Yang SQ, Tian WL (2019) Crack coalescence behavior of sandstone specimen containing two pre-existing flaws under different confining pressures. *Theor Appl Fract Mech* 99:118–130
- Janeiro RP, Einstein HH (2010) Experimental study of the cracking behavior of specimens containing inclusions (under uniaxial compression). *Int J Fract* 164(1):83–102
- Lee H, Jeon S (2011) An experimental and numerical study of fracture coalescence in pre-cracked specimens under uniaxial compression. *Int J Solids Struct* 48(6):979–999
- Lee J, Ha YD, Hong JW (2017) Crack coalescence morphology in rock-like material under compression. *Int J Fract* 203(1–2):211–236
- Li TC, Lyu LX, Zhang SL, Sun JC (2015) Development and application of a statistical constitutive model of damaged rock affected by the load-bearing capacity of damaged elements. *J Zhejiang Univ Sci A* 16(8):644–655
- Li WT, Yang N, Mei YC, Zhang YH, Wang L, Ma HY (2020) Experimental investigation of the compression-bending property of the casing joints in a concrete filled steel tubular supporting arch for tunnel engineering. *Tunn Undergr Space Technol* 96:103184. <https://doi.org/10.1016/j.tust.2019.103184>
- Lu ZD, Chen CX, Feng XT, Zhang YL (2014) Strength failure and crack coalescence behavior of sandstone containing single pre-cut fissure under coupled stress, fluid flow and changing chemical environment. *J Cent South Univ* 21(3):1176–1183
- Lu YL, Wang LG, Elsworth D (2015) Uniaxial strength and failure in sandstone containing a pre-existing 3-D surface flaw. *Int J Fract* 194(1):59–79
- Martin CD, Chandler NA (1994) The progressive fracture of lac du bonnet granite. *Int J Rock Mech Min Sci Geomech Abstr* 31(6):643–659
- Morgan SP, Johnson C, Einstein HH (2013) Cracking processes in Barre granite: fracture process zones and crack coalescence. *Int J Fract* 180(2):177–204
- Oda M, Takemura T, Aoki T (2002) Damage growth and permeability change in triaxial compression tests of Inada granite. *Mech Mater* 34(6):313–331
- Park CH, Bobet A (2009) Crack coalescence in specimens with open and closed flaws: a comparison. *Int J Rock Mech Min Sci* 46(5):819–829
- Park CH, Bobet A (2010) Crack initiation, propagation and coalescence from frictional flaws in uniaxial compression. *Eng Fract Mech* 77(14):2727–2748
- Prudencio M, Van SJM (2007) Strength and failure modes of rock mass models with non-persistent joints. *Int J Rock Mech Min Sci* 44(6):890–902
- Sun Q, Xue L, Zhu SY (2015) Permeability evolution and rock brittle failure. *Acta Geophys* 63(4):978–999
- Tang Y, Okubo S, Xu J, Peng SJ (2019) Progressive failure behaviors and crack evolution of rocks under triaxial compression by 3D digital image correlation. *Eng Geol* 249:172–185
- Wang HL, Xu WY, Shao JF (2014a) Experimental researches on hydro-mechanical properties of altered rock under confining pressures. *Rock Mech Rock Eng* 47(2):485–493
- Wang SY, Sloan SW, Sheng DC, Yang SQ, Tang CA (2014b) Numerical study of failure behaviour of pre-cracked rock specimens under conventional triaxial compression. *Int J Solids Struct* 51(5):1132–1148
- Wang L, Liu JF, Pei JL, Xu HN, Bian Y (2015) Mechanical and permeability characteristics of rock under hydro-mechanical coupling conditions. *Environ Earth Sci* 73(10):5987–5996
- Wang HL, Xu WY, Lu ZB, Chao ZM, Meng QX (2016a) Dependency of hydromechanical properties of monzonitic granite on confining pressure and fluid pressure under compression. *Int J Mod Phys B*. <https://doi.org/10.1142/S0217979216500867>
- Wang HL, Xu WY, Jia CJ, Cai M, Meng QX (2016b) Experimental research on permeability evolution with microcrack development in sandstone under different fluid pressures. *J Geotech Geoenviron*. [https://doi.org/10.1061/\(asce\)gt.1943-5606.0001462](https://doi.org/10.1061/(asce)gt.1943-5606.0001462)

- Wang YL, Tang JX, Dai ZY, Yi T (2018) Experimental study on mechanical properties and failure modes of low-strength rock samples containing different fissures under uniaxial compression. *Eng Fract Mech* 197:1–20
- Wang G, Han W, Jiang YJ, Luan HJ, Wang K (2019) Coupling analysis for rock mass supported with CMC or CFC rockbolts based on viscoelastic method. *Rock Mech Rock Eng* 52(11):4565–4588
- Wong LNY, Einstein HH (2009) Systematic evaluation of cracking behavior in specimens containing single flaws under uniaxial compression. *Int J Rock Mech Min Sci* 46(2):239–249
- Wong LNY, Li HQ (2013) Numerical study on coalescence of two pre-existing coplanar flaws in rock. *Int J Solids Struct* 50(22–23):3685–3706
- Wu JY, Feng MM, Han GS, Yao BY, Ni XY (2019) Loading rate and confining pressure effect on dilatancy, acoustic emission, and failure characteristics of fissured rock with two pre-existing flaws. *C R Mecanique* 347(1):62–89
- Wyckoff RD, Botsset HG, Muskat M, Reed DW (1933) The measurement of the permeability of porous media for homogeneous fluid. *Rev Sci Instrum* 4(7):394–405
- Yang SQ, Huang YH (2017) An experimental study on deformation and failure mechanical behavior of granite containing a single fissure under different confining pressures. *Environ Earth Sci* 76(10):1–22
- Yang SQ, Jing HW (2011) Strength failure and crack coalescence behavior of brittle sandstone samples containing a single fissure under uniaxial compression. *Int J Fract* 168(2):227–250
- Yang SQ, Jiang YZ, Xu WY, Chen XQ (2008) Experimental investigation on strength and failure behavior of pre-cracked marble under conventional triaxial compression. *Int J Solids Struct* 45(17):4796–4819
- Yang SQ, Huang YH, Tian WL, Zhu JB (2017) An experimental investigation on strength, deformation and crack evolution behavior of sandstone containing two oval flaws under uniaxial compression. *Eng Geol* 217:38–48
- Yang SQ, Huang YH, Ranjith PG (2018) Failure mechanical and acoustic behavior of brine saturated-sandstone containing two pre-existing flaws under different confining pressures. *Eng Fract Mech* 193:108–121
- Yin P, Wong RHC, Chau KT (2014) Coalescence of two parallel pre-existing surface cracks in granite. *Int J Rock Mech Min Sci* 68:66–84
- Yu J, Chen SJ, Chen X, Zhang YZ, Cai YY (2015) Experimental investigation on mechanical properties and permeability evolution of red sandstone after heat treatments. *J Zhejiang Univ Sci A* 16(9):749–759
- Zeng W, Yang SQ, Tian WL, Wen K (2018) Numerical investigation on permeability evolution behavior of rock by an improved flow-coupling algorithm in particle flow code. *J Cent South Univ* 25(6):1367–1385
- Zhang R, Jiang ZQ, Sun Q, Zhu SY (2013) The relationship between the deformation mechanism and permeability on brittle rock. *Nat Hazards* 66(2):1179–1187
- Zhao YL, Zhang LY, Wang WJ, Pu CZ, Wan W, Tang JZ (2016) Cracking and stress–strain behavior of rock-like material containing two flaws under uniaxial compression. *Rock Mech Rock Eng* 49(7):2665–2687
- Zhao YL, Tang JZ, Chen Y, Zhang LY, Wang WJ, Wan W, Liao JP (2017) Hydromechanical coupling tests for mechanical and permeability characteristics of fractured limestone in complete stress–strain process. *Environ Earth Sci* 76(1):24
- Zhao C, Niu JL, Zhang QZ, Zhao CF, Zhou YM (2019) Failure characteristics of rock-like materials with single flaws under uniaxial compression. *Bull Eng Geol Environ* 78(1):593–603
- Zhou XP, Cheng H, Feng YF (2014) An experimental study of crack coalescence behaviour in rock-like materials containing multiple flaws under uniaxial compression. *Rock Mech Rock Eng* 47(6):1961–1986
- Zhou T, Zhu JB, Ju Y, Xie HP (2019) Volumetric fracturing behavior of 3D printed artificial rocks containing single and double 3D internal flaws under static uniaxial compression. *Eng Fract Mech* 205:190–204

Publisher's Note Springer Nature remains neutral with regard to jurisdictional claims in published maps and institutional affiliations.